Journal of Materials Chemistry B

ROYAL SOCIETY OF CHEMISTRY

PAPER

View Article Online
View Journal

Open Access Article. Published on 11 February 2026. Downloaded on 2/25/2026 7:32:26 AM.
This article is licensed under a Creative Commons Attribution-NonCommercial 3.0 Unported Licence.

Check for updates

Cite this: DOI: 10.1039/d5tb02465j

Stable ultrabright nanoprobes for two-photon excitation microscopy based on octupolar merocyanine-loaded nanovesicles

Sara Garrido-Rodríguez,†[ab] Yevgen M. Poronik,†[c] Andrea Delledonne,†[d] Silvia Pescina,[e] Guillem Vargas-Nadal,[ab] Judit Morla-Folch,[a] Ottavia Racchi,[d] Francesco Di Maiolo,[d] Nora Ventosa,[abf] Cristina Sissa,*[d] Daniel T. Gryko*[c] and Mariana Köber*[ab]

Two-photon microscopy is a powerful technique for deep-tissue and *in vivo* fluorescence imaging, yet its full potential is often constrained by the low two-photon absorption efficiency of conventional fluorophores. In this work, for the first time non-liposomal, unilamellar quatsome nanovesicles were loaded with octupolar fluorophores. Molecular engineering of centrosymmetric merocyanines led to dyes emitting in the 600–700 nm range with a fluorescence quantum yield ≈ 0.16 in polar solvents. Centrosymmetric architecture made it possible to perform heretofore unachievable systematic investigation of the impact of hydrophobic and hydrophilic (triethylene glycol) moieties on the stability of nanocarriers. It was discovered that two long alkyl chains are prerequisites to achieving stable incorporation of dyes within nanovesicles. Through systematic formulation screening, we identified a lead nanoprobe exhibiting high brightness, in the order of 10^7 M^{-1} cm^{-1}, combined with strong and broad nonlinear optical properties leading to large two-photon brightness, in the order of 10^4 GM, in a highly stable nanoparticle. The performance of these very bright nanoprobes in two-photon microscopy was assessed in *ex vivo* permeation studies using porcine tissues, demonstrating their potential for bioimaging applications. This work underscores the synergy between molecular design and nanocarrier engineering in advancing next-generation fluorescent probes for nonlinear optical imaging.

Received 5th November 2025,
Accepted 26th January 2026

DOI: 10.1039/d5tb02465j

rsc.li/materials-b

1. Introduction

Two-photon microscopy (2PM) has emerged as an innovative tool for fluorescence imaging of biological structures, owing to its ability to excite fluorophores and reconstruct 3D images.[1–4] Unlike conventional fluorescence microscopy techniques that rely on single-photon excitation, 2PM typically exploits the simultaneous absorption of two photons to excite fluorophores with infrared light, instead of UV or visible light. This nonlinear excitation process, confined to the focal plane where the photon density reaches its maximum, effectively minimizes out-of-focus fluorescence, intrinsically providing three-dimensional resolution, of the order of 0.5 μm in the *x*–*y* plane and of 1 μm in the *z* direction.[1,4,5] Additionally, the use of infrared excitation reduces fluorophore bleaching, enhances tissue penetration depth up to 1–2 mm and increases the signal-to-noise ratio, making 2PM particularly effective for applications like deep-tissue and *in vivo* imaging, which may be challenging for conventional confocal microscopy.[1,3,6]

Classical one-photon-absorption (1PA) chromophores, commonly used in conventional fluorescence microscopy techniques, are usually less efficient for 2PM, as they typically exhibit relatively low two-photon-absorption cross-sections (σ_2) within the biologically relevant spectral window (650–1000 nm).[7,8] Therefore, the development of more efficient two-photon-active chromophores with high σ_2 values, along with desirable optical and chemical properties—such as long-term stability, high brightness, and biocompatibility—is crucial to fully exploit the potential of 2PM in biological imaging.[7]

The design and application of fluorophores with nonlinear optical (NLO) properties have attracted significant attention in

[a] Institut de Ciència de Materials de Barcelona (ICMAB-CSIC), Campus UAB, Cerdanyola del Vallès, Spain. E-mail: mkober@icmab.es
[b] Centro de Investigación Biomédica en Red: Bioingeniería, Biomateriales y Nanomedicina (CIBER-BBN), Spain
[c] Institute of Organic Chemistry of the Polish Academy of Sciences, 44/52 Kasprzaka Str., 01-224 Warsaw, Poland. E-mail: daniel.gryko@icho.edu.pl
[d] Department of Chemistry, Life Sciences and Environmental Sustainability, University of Parma, Parco Area delle Scienze 17/A, 43124 Parma, Italy. E-mail: cristina.sissa@unipr.it
[e] ADDRes Lab, Department of Food and Drug, University of Parma, Parco Area delle Scienze, 27/A, Parma, Italy
[f] Nanomol Technologies S.L., Campus UAB, Bellaterra 08193, Spain
† These authors contributed equally.

Open Access Article. Published on 11 February 2026. Downloaded on 2/25/2026 7:32:26 AM.
This article is licensed under a Creative Commons Attribution-NonCommercial 3.0 Unported Licence.

recent years due to their potential in various advanced imaging techniques.[7,9–12] Many of these fluorophores are particularly well-suited for 2PM, making them valuable tools for fluorescence-based imaging.[7–9] It is well established that among various molecular architectures quadrupolar and especially octupolar dyes have much larger two-photon absorption cross-sections (σ_2) compared with their dipolar analogues,[13–19] and octupolar fluorophores designed for bioimaging have shown good biocompatibility.[20] Among NLO dyes, merocyanine chromophores exhibit stronger polarization along the conjugation chain than polyenes.[21] In this light, we resolved to employ in our investigation the octupolar merocyanines framework which was reported to possess two-photon absorption cross sections in the range of 1300–2300 GM, reasonably strong fluorescence, good solubility and emission that falls within the first biological transparency window.[7]

Despite their interesting NLO properties, these fluorophores are highly hydrophobic, making them insoluble and unstable in aqueous environments. A promising strategy to stabilize these hydrophobic fluorophores and preserve their optical properties in aqueous environments involves their encapsulation within nanoparticles.[22] This approach can protect the fluorophores from reactive species, enhance biocompatibility, enhance brightness,[23] and enable targeted delivery through functionalization of the nanovesicle surface.

In this work, we employed non-liposomal, lipid-based quatsome (QS) nanovesicles as nanocarriers for fluorophores with NLO properties. These small unilamellar vesicles, composed of quaternary ammonium surfactants and sterols,[24] exhibit high homogeneity in morphology and size, along with exceptional colloidal stability in aqueous media.[25–29] Quatsomes are a versatile platform for the incorporation and delivery of many different (bio-)molecules *via* hydrophobic and/or electrostatic interactions.[28,30,31] Previous studies have demonstrated the potential of QS to carry a variety of fluorescent dyes in their membranes, leading to highly stable, ultrabright nanoparticles.[32–37] In addition, QS have been reported to exhibit efficient cellular internalization while preserving nanoprobe integrity and cell viability,[33,37] highlighting their suitability as biocompatible nanocarriers in biological systems. Notably, in a previous study, QS composed of cholesterol and MKC were developed for *in vivo* use, showing no histopathological alterations or toxicity in any of the organs with major nanoparticle accumulation upon intravenous administration in mice.[29] The present work employs this same base formulation, which was subsequently optimized to enhance its suitability for two-photon excitation microscopy applications.

Herein, we present the development of stable nanoprobes for two-photon absorption (2PA) microscopy, based on octupolar merocyanine dye-loaded quatsome nanovesicles (Fig. 1). A family of octupolar merocyanine dyes, incorporating varying numbers of alkyl chains and triethylene glycol units (Fig. 1A), was synthesized and spectroscopically characterized. A systematic screening and in-depth characterization of fluorophore-loaded quatsome formulations was performed to identify the most promising 2PM nanoprobes. The selected formulation was then evaluated in *ex vivo* permeation experiments using porcine sclera as a biologically relevant model.

2. Results and discussion

2.1. Design of chromophores for 2PA nanoprobe development

To achieve intense 2PA cross sections as well as strong fluorescence in the red spectral region we designed a series of octupolar chromophores possessing a merocyanine structure. Efficient incorporation in the QS membrane requires dyes to possess, at the same time, hydrophobic moieties, that are compatible with the membrane components, and hydrophilic groups to promote interaction with the QS surface, which is exposed to water.[17–24] In this context, an octupolar structure serves as an optimal platform, as it enables the introduction of three functionalities, one on each arm, for the proper integration into the QS structure.

2.2. Synthesis of octupolar merocyanine dyes containing alkyl and triglycol chains (dyes 4–7)

Octupolar merocyanines are commonly synthesized through the direct condensation of methyl heterocyclic bases or salts and phloroglucinol trialdehyde.[7] This approach is primarily suited for symmetrical octupoles. However, for asymmetrical products, the direct method would yield four different products in a statistical ratio, resulting in a complex reaction mixture that makes purification extremely challenging. To overcome these purification issues, we developed a modified approach for asymmetric octupolar chromophores, as shown in Scheme 1. We found that when the reaction was performed in boiling toluene or xylene, it predominantly resulted in the formation of the double condensation product rather than the triple condensation product obtained in pyridine.[7] Following this approach, we synthesized a pair of double condensation products, **3a** and **3b**, starting from heterocyclic bases **2a** and **2b**, respectively. Our strategy was to carry out cross-condensations between the half-product **3a** and counter base **2b**, as well as the reversed combination of **3b** and **2a** to obtain asymmetric octupolar dyes, respectively. However, we discovered that the process was more complex than initially expected. The reaction between **3a** and **2b** predominantly yielded product **5**, accompanied by minor amounts of side products **4** and **6**, as well as trace amounts of **7**. Similarly, the reversed condensation of **3b** and **2a** resulted in a mixture where **6** was the major product, while **5** and **7** were obtained in minor amounts, with **4** detected only in trace quantities. The formation of side products suggests that the condensation reaction is reversible, leading to the generation of merocyanine dyes with different combinations of alkyl and triglycol chains within the same reaction. A similar phenomenon, known as 'scrambling' has been observed in porphyrin chemistry.[38] Ultimately, we were able to isolate all four products (**4–7**) from the reaction mixture for use in quatsome formulation experiments.

2.3. Spectroscopic characterization of dyes 4–7

Compounds **4–7** show an intense absorbance band around 600 nm and a weaker band at higher energy ($\approx$450 nm), as shown in Fig. 2 for compound **5** and in Fig. S1 for **4**, **6** and **7**.

The emission spectra of all four dyes show resolved vibronic structures, with the 0–0 transition being the most intense. Emission spectra extend up to 700 nm, which falls within the first biological transparency window, thus making them particularly attractive for

 This journal is © The Royal Society of Chemistry 2026

Open Access Article. Published on 11 February 2026. Downloaded on 2/25/2026 7:32:26 AM.
This article is licensed under a Creative Commons Attribution-NonCommercial 3.0 Unported Licence.

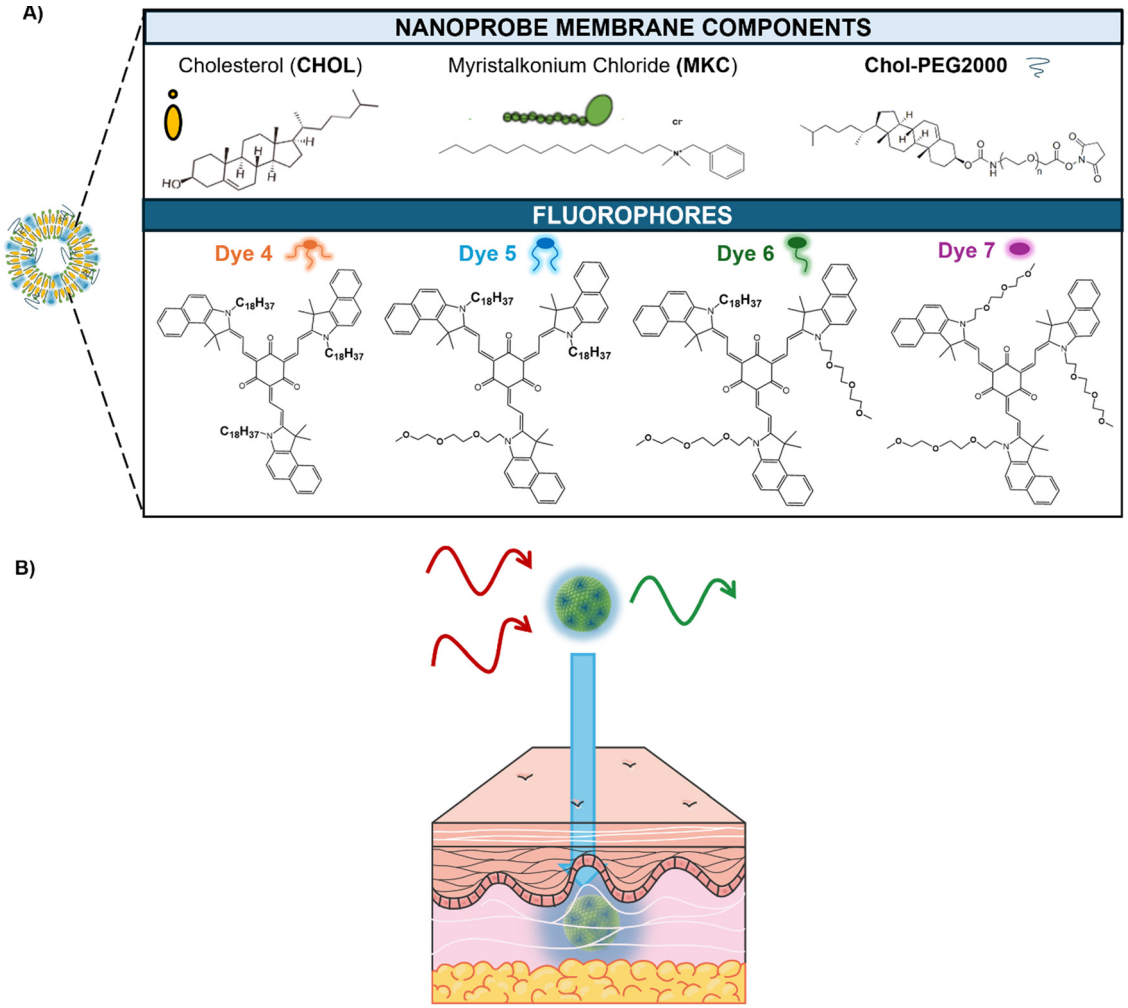

Fig. 1 Schematic representation of octupolar merocyanine-loaded quatsome nanovesicles. (A) Molecular structure and schematic representation of the different membrane components and octupolar merocyanine dyes employed for the development of stable 2PA nanoprobes. (B) Schematic representation of *ex vivo* permeation experiments of 2PM nanoprobes based on quatsomes loaded with dye **5** performed on isolated tissue.

bioimaging applications (Fig. 1 and Table 1). Moreover, they exhibit a high molar extinction coefficient (>200 000 M^{-1} cm^{-1}), good fluorescence quantum yield (>10% in most solvents), and a moderate Stokes shift (≈600 cm^{-1}), confirming their strong potential for use in fluorescence microscopy. Compared with our earlier octupolar merocyanines,[7,39] dyes **4–7** have *ca.* 25 nm red shifted absorption and emission and slightly lower emission intensity. Emission was also characterized in terms of fluorescence lifetimes (Table 1), which ranged from 0.4 to 0.8 ns, further confirming that the emissive process corresponds to fluorescence. The absorption spectra exhibit weak positive solvatochromism, in agreement with previous reports on octupolar merocyanine dyes.[7] Such behavior is generally unexpected for octupolar systems with D_{3h} symmetry, owing to the absence of a permanent dipole moment in the ground state.[40] In the present case, the structural flexibility of the octupolar framework likely induces a small ground-state dipole moment, accounting for the modest solvatochromic shift observed in absorption (≈600 cm^{-1} upon changing the solvent from cyclohexane to ethanol). The emission spectra display a more pronounced solvatochromic response (≈800 cm^{-1} over the same solvent range), indicating increased stabilization of the excited state in polar environments and suggesting a slightly larger permanent dipole moment in the first excited state compared to the ground state. Both the fluorescence quantum yield and lifetimes increase with solvent polarity. All four dyes were found to be insoluble in aqueous media without the addition of organic co-solvents, confirming their strong hydrophobic character. For this reason, the dyes were considered for encapsulation in QSs as a strategy to enable stable dispersion in aqueous media and preserve their optical properties.

3. Development of octupolar merocyanine dye-based 2PA nanoprobes

3.1. Impact of alkyl and triglycol chains on dye loading into quatsome nanovesicles

To develop 2PA-nanoprobes that are compatible for *in vivo* imaging, we have chosen a base formulation of quatsomes composed

Open Access Article. Published on 11 February 2026. Downloaded on 2/25/2026 7:32:26 AM.
This article is licensed under a Creative Commons Attribution-NonCommercial 3.0 Unported Licence.

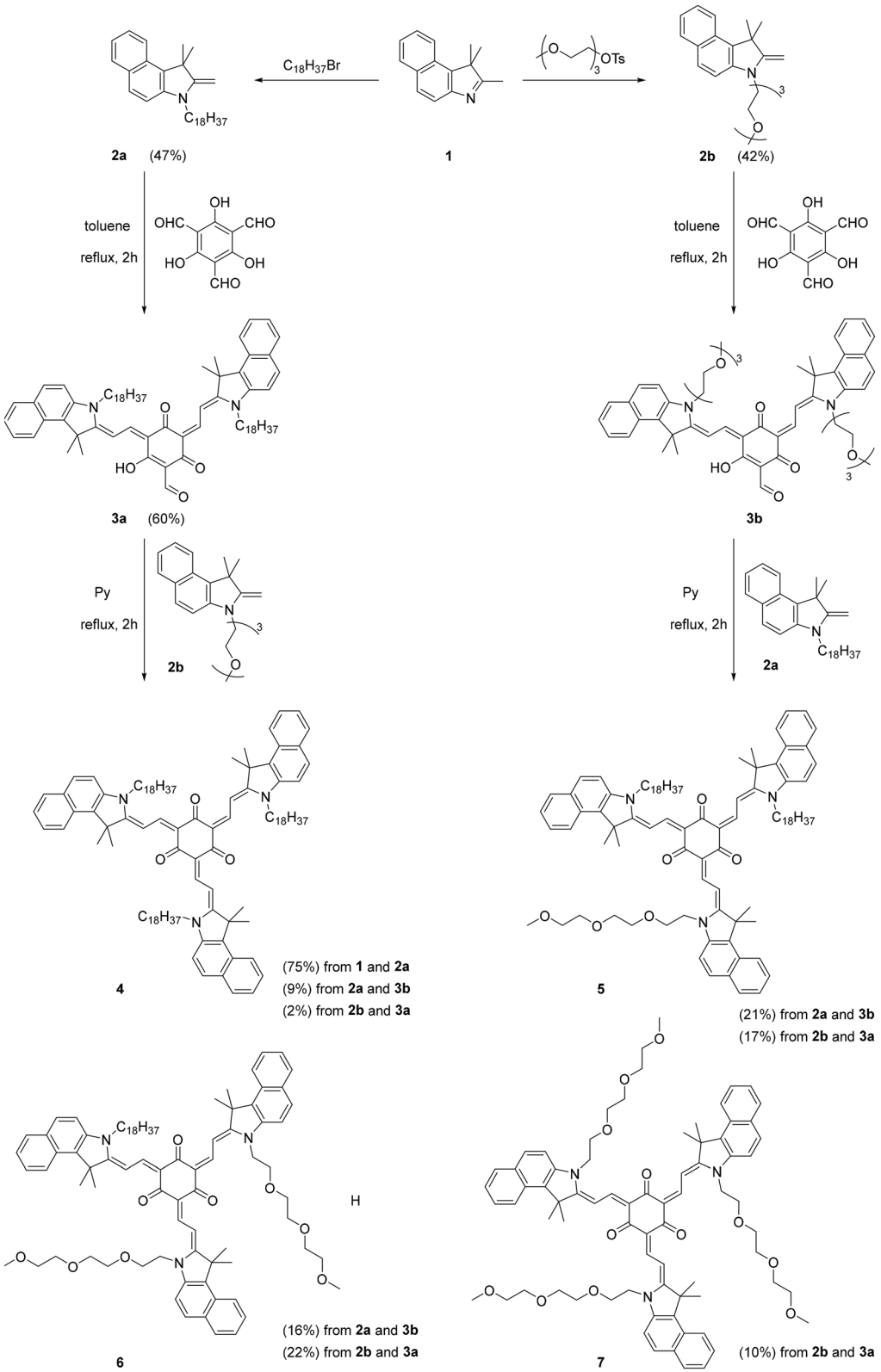

Scheme 1 The synthesis of octupolar merocyanine dyes **4–7**, containing different numbers of C18 alkyl and triglycol chains.

of cholesterol (CHOL) and myristalkonium chloride (MKC), as previous studies in mice showed no detectable histopathological alterations or signs of toxicity following intravenous administration.[29] To enhance the stability of the dye-encapsulating nanoformulation, CHOL-PEG2000 was added to the formulation. QS dispersed in PBS 100 mM were prepared using an

 This journal is © The Royal Society of Chemistry 2026

Open Access Article. Published on 11 February 2026. Downloaded on 2/25/2026 7:32:26 AM.
This article is licensed under a Creative Commons Attribution-NonCommercial 3.0 Unported Licence.

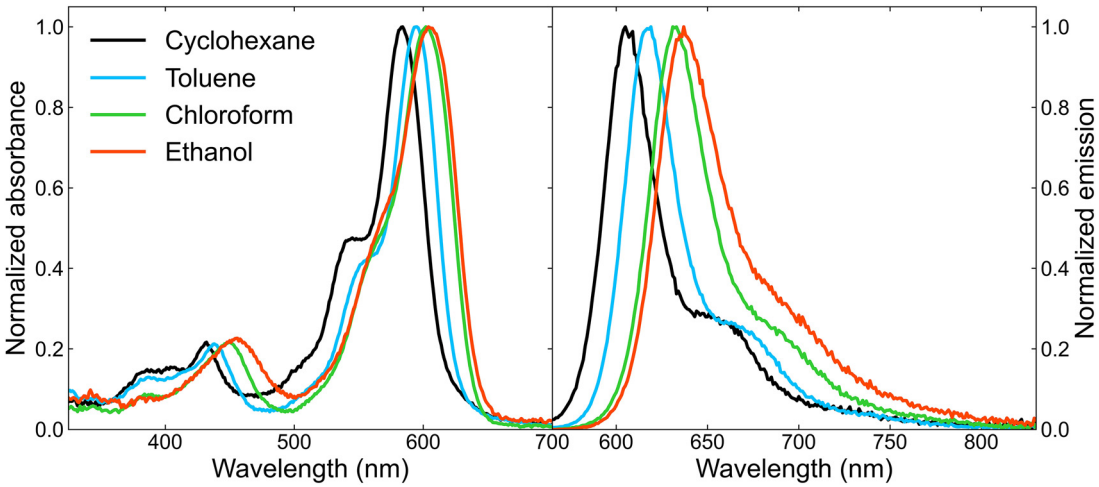

Fig. 2 Normalized absorbance (left panel) and emission spectra (right panel) of dye **5** in solvents of different polarity. All the emission spectra were obtained by exciting the sample at 560 nm.

Table 1 Spectroscopic characterization of dyes **4–7**

Dye ID	Solvent	λ_{abs}/nm	$\varepsilon \times 10^{-5}$/$M^{-1}$ cm^{-1}	λ_{em}/nm	$\bar{\nu}^a$/cm^{-1}	Φ_f^b	τ^c/ns
4	Cyclohexane	584	—	604	567	0.09	0.40
	Toluene	594	2.31	616	601	0.16	0.55
	$CHCl_3$	603	—	632	761	0.15	0.64
	C_2H_5OH	605	2.18	638	855	0.17	0.82
5	Cyclohexane	584	—	605	594	0.06	0.41
	Toluene	594	2.37	615	575	0.15	0.59
	$CHCl_3$	602	—	631	763	0.15	0.63
	C_2H_5OH	605	2.20	638	855	0.18	0.79
6	Cyclohexane	583	—	608	705	0.07	0.41
	Toluene	594	2.26	619	680	0.15	0.58
	$CHCl_3$	603	—	634	811	0.15	0.66
	C_2H_5OH	605	2.19	640	904	0.16	0.79
7	Cyclohexane	581	—	610	818	0.05	0.41
	Toluene	594	2.25	619	680	0.15	0.57
	$CHCl_3$	601	—	632	816	0.15	0.64
	C_2H_5OH	605	2.17	641	928	0.15	0.78

[a] Stokes shift. [b] Fluorescence quantum yields determined using fluorescein in NaOH 0.1 M as a reference standard, as described in the Materials and Methods Section. [c] Fluorescence lifetimes obtained by monoexponential reconvolution fitting of the fluorescence decay curves acquired at the emission maxima.

equimolar ratio of MKC/CHOL, 2.9% mol of CHOL-PEG2000 (ratio 1 : 1 : 0.06) and one of the four different merocyanine dyes (**4**, **5**, **6** and **7**) (the initial compositions are provided in detail in Tables S1 and S2). For the QS productions we have used a scalable, environmentally friendly method based on compressed CO_2 (DELOS-SUSP),[41–43] and all formulations prepared in PBS were diafiltered to remove the ethanol and any non-entrapped hydrophilic components (see the Materials and Methods Section for details, Fig. S2).

All four nanovesicle dispersions presented hydrodynamic diameters (d_{hyd}) below 200 nm (Fig. 3A), which were slightly smaller (≈110 nm) in the presence of dyes **4** and **5** (containing three and two C18 alkyl chains, respectively) than in the presence of dyes **6** and **7** (≈160 nm). In all cases the size dispersion ($Đ$) was below 0.4, with dye 7-loaded QS showing a slightly higher $Đ$ than the rest of the formulations. All four formulations displayed a unilamellar morphology and predominantly spherical and prolate shapes, except Q-7 which exhibited rather peanut-like shapes, possibly due to a certain perturbation of the supramolecular self-assembly in the presence of dye **7** which is void of any alkyl chains (Fig. 3E). All formulations exhibited a low ζ-potential (+8 to +12 mV), which can be attributed to the presence of CHOL-PEG2000 on the nanovesicle surface (Fig. 3B). Size and ζ-potential values of the four formulations are in line with data obtained for similar QS nanovesicle dispersions.

However, absorption and emission spectra (Fig. 3C and D) showed large differences between nanoparticle dispersions containing dyes **4** and **5**, which closely resembled those of the free dyes dissolved in ethanol, indicating effective encapsulation with minimal perturbation of their optical properties, and those containing dyes **6** and **7**, which exhibited negligible fluorescence emission, suggesting poor encapsulation and the formation of non-emissive species due to aggregation either inside the QS membrane or in the surrounding aqueous environment. Upon disruption of the nanoparticles by dilution in ethanol, the emission spectra were restored (Fig. S3), confirming that the dyes had not been properly stabilized within the nanovesicle. Furthermore, the absorbance spectra for these formulations showed markedly reduced overall intensity along with altered spectral profiles, further supporting inefficient dye incorporation. Comparing dyes **4** and **5**, both exhibit comparable absorbance and emission spectra when normalized to their respective dye loadings (Table S3).

These findings highlight the critical role of hydrophobic alkyl chains in promoting the effective entrapment of the fluorophores within the nanovesicle, due to hydrophobic interactions with the hydrophobic vesicle bilayer, leading to the preservation of the dyes' optical properties. A minimum of two C18 alkyl chains were required for a stable entrapment into the nanoprobe bilayer, resulting in adequate fluorescence emission profiles. As dye **4** and dye **5** showed comparable characteristics,

Open Access Article. Published on 11 February 2026. Downloaded on 2/25/2026 7:32:26 AM.
This article is licensed under a Creative Commons Attribution-NonCommercial 3.0 Unported Licence.

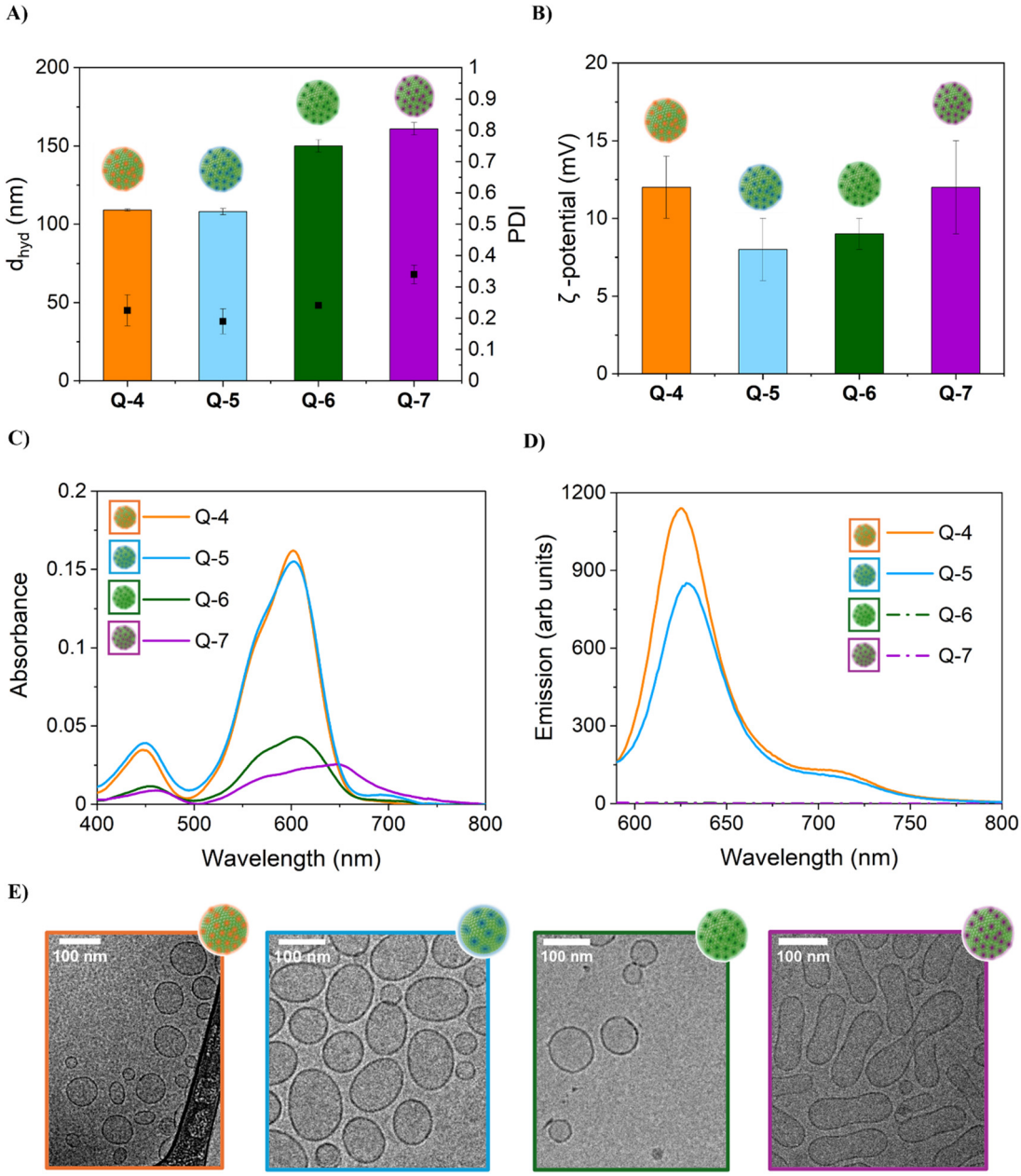

Fig. 3 Impact of alkyl and triglycol chains on octupolar merocyanine dye loading into quatsome nanovesicles. (A) Hydrodynamic diameter and PDI of QS dispersions containing dyes **4**, **5**, **6**, and **7**, obtained from DLS measurements in PBS. (B) Corresponding ζ-potential, obtained from ELS measurements in PBS. (C) Absorbance and (D) emission spectra (λ_{exc} = 570 nm). (E) Corresponding morphological appearance shown in representative cryo-TEM images of Q-4 (orange), Q-5 (blue), Q-6 (green) and Q-7 (purple).

we performed further in-depth studies with only one of the two dyes, namely dye **5** (two C18 alkyl chains).

3.2. Impact of dye loading on nanoprobe brightness

Once dye **5** was selected due to its favorable entrapment in QS nanovesicles, different dye loadings per nanoparticle were screened to identify the loading that yields maximal brightness. Increased loadings oftentimes lead to a reduction in quantum yield that may outweigh – at a certain threshold value – the increase in brightness obtained through an increase in fluorophore loading per particle.[36] Furthermore, increased loadings may affect the nanoprobe morphology and size, as well as its colloidal stability, amongst others. To assess the impact of octupolar merocyanine dye **5** loading into QS, QS dispersions containing three different dye concentrations (1 μM, 7 μM, and 36 μM) were prepared (Fig. 4A), referenced as Q-**5**-1, Q-**5**-7, and Q-**5**-36, and a comprehensive characterization was carried out with respect to their physico-chemical properties, photo-physical characteristics, and two-photon absorption cross section.

3.2.1. Physico-chemical characterization. All QS prepared at the three different loadings (Q-**5**-1, Q-**5**-7, and Q-**5**-36) yielded quatsome dispersions presenting a monomodal size distribution

 This journal is © The Royal Society of Chemistry 2026

Open Access Article. Published on 11 February 2026. Downloaded on 2/25/2026 7:32:26 AM.
This article is licensed under a Creative Commons Attribution-NonCommercial 3.0 Unported Licence.

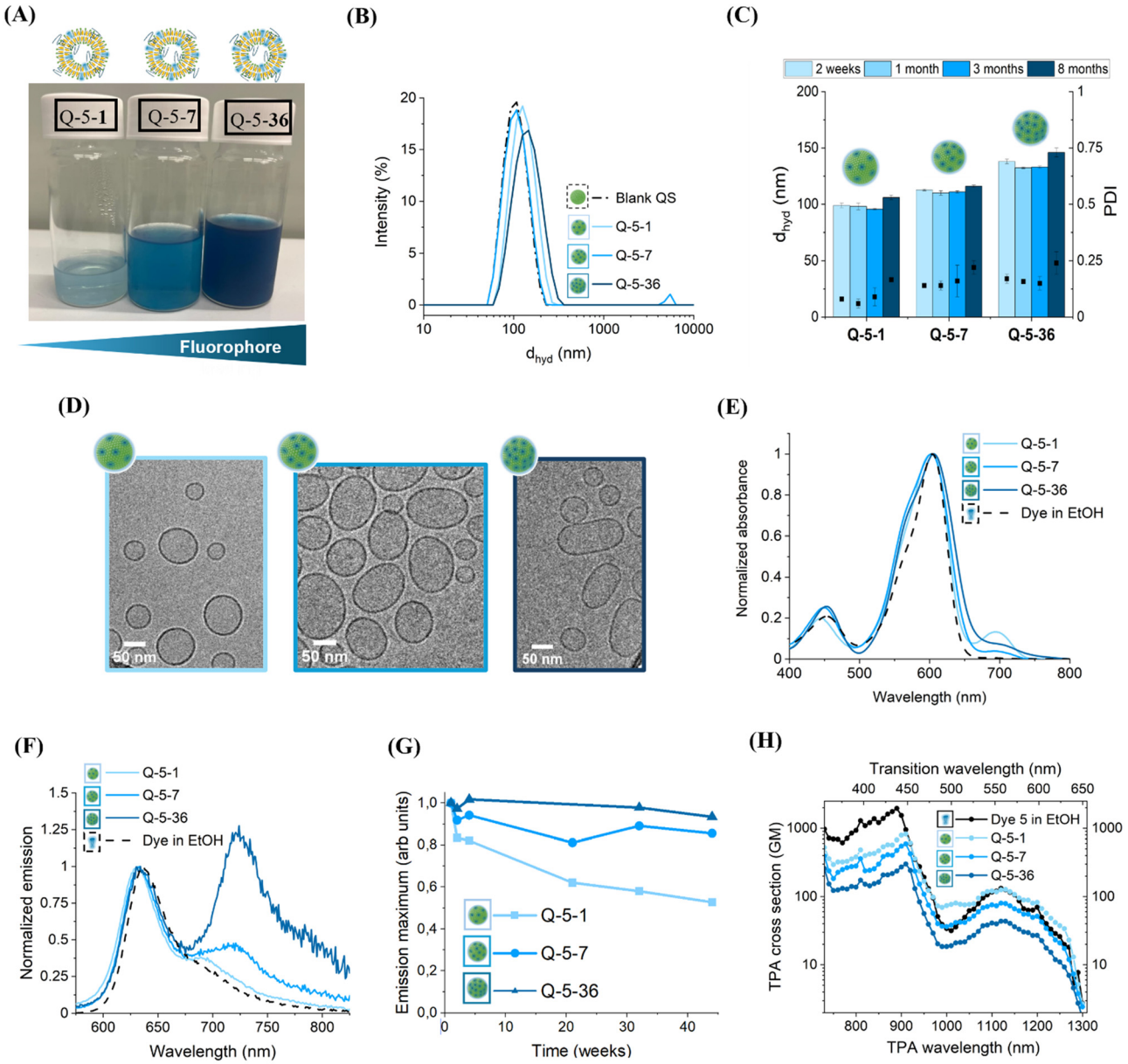

Fig. 4 Impact of dye loading on the physico-chemical particle characteristics, colloidal stability, absorbance and emission spectra, and two-photon absorption cross section, of QS dispersions containing octupolar merocyanine dye **5** (with two C18 alkyl chains and one triglycol). (A) Macroscopic appearance of dye-loaded quatsome dispersions, with increasing dye loading from left to right. (B) Size distributions (intensity weighted) obtained from DLS measurements. (C) Evolution of d_{hyd} over an 8 month-period. (D) Corresponding morphological appearance shown in representative cryo-TEM images. (E) Normalized absorbance spectra of QS formulations in PBS and free dye in ethanol. (F) Normalized emission spectra (λ_{exc} = 570 nm) of free dye in ethanol (dashed black line) and dye-loaded QS dispersions in PBS (solid blue lines; darker shadings correspond to increasing dye loadings). (G) Evolution of the maximum emission of dye-loaded QS over 8 months. (H) Absolute TPA cross section of the free dye **5** in EtOH (black) and dye **5**-loaded QS dispersions at different dye loadings (blue).

with a mean hydrodynamic diameter slightly above 100 nm and a highly homogeneous unilamellar morphology (Fig. 4B, D and Table 2). At the highest dye loading (Q-**5**-36) nanovesicles were slightly larger (~140 nm) and showed a more pronounced elongation. ζ-potentials were not affected by higher loadings, and showed slightly positive values (Table 2), resulting from the cationic head group of MKC that is partially shielded due to the presence of CHOL-PEG2000. Batch-to-batch reproducibility was very high, with no significant variations observed in either size or ζ-potential (Fig. S5A and B). Colloidal stability, monitored over an 8 month-period, remained high for all three dyes loadings, with no significant changes observed in size, size dispersion (*Đ*), or ζ-potential (Fig. 4C and Fig. S6).

3.2.2. Spectroscopic characterization. For all three loadings, absorption and emission spectra of **5**-loaded QS dispersions closely resembled those of dye **5** solubilized in ethanol (Fig. 4E and F). This is indicative of successful dye entrapment in the vesicle membrane, given that dye **5** dispersed in water

Open Access Article. Published on 11 February 2026. Downloaded on 2/25/2026 7:32:26 AM.
This article is licensed under a Creative Commons Attribution-NonCommercial 3.0 Unported Licence.

(with a small amount of organic solvent, *e.g.* 2.5% DMSO) shows clear signs of H-type aggregation, including a broadened absorption spectrum and weak, red-shifted emission with a quantum yield below 1% (Fig. S7).[44,45] The absorption maximum remained at a similar wavelength, but the band around 600 nm was broader in the QS samples, suggesting some structural disorder or residual aggregation within the quatsome membrane. Absorbance and emission spectra remained largely unchanged after 8 months at the intermediate (QS-5-7) and highest loading (QS-5-36), with only a slight reduction (∼10%) observed at the emission peak, whereas the lowest loading showed a moderate reduction (∼35%) in emission (Fig. 4G and Fig. S6).

QS prepared at low dye loading (Q-5-1) displayed an additional absorption band at 700 nm, which could be attributed to dye aggregation or photodegradation/photoactivated species. On the other hand, a distinct 715 nm emission band emerged and became more intense with increasing dye loading. As the absorption band remained present upon disruption of the nanovesicle structure by diluting the suspensions in pure ethanol (1 : 30 v/v), dye aggregation was ruled out as the origin of this additional band (Fig. S9). Prolonged exposure to ambient light led to an increase of the absorption band at 700 nm (Fig. S10 and S11), suggesting the presence of photogenerated species. This is further supported by experiments performed at different time points following excitation at 630 nm (Fig. S11). This behavior has been previously reported for similar merocyanine systems and was attributed to irreversible photoactivated reactions.[46] To test this hypothesis, density-functional theory (DFT) and time-dependent density-functional theory (TDDFT) calculations were performed on different conformers (see the Materials and Methods section and Fig. S12 and S13 for full details). These calculations show that the lowest-energy electronic transitions are consistently red-shifted for the cisoid conformer relative to the transoid one. In both a single-arm model and the full three-arm dye, the $S_0 \rightarrow S_1$ excitation, primarily HOMO → LUMO in characteristic, decreases in energy in the cisoid geometry (0.08 eV for the single-arm analogue), and the same trend is observed for the next-lowest excited state as well as for the higher-lying dark states. These results support the idea that a photo-induced *cis–trans* isomerization could be responsible for the absorption band observed at 700 nm.

As these spectral features were more pronounced after diafiltration (Fig. S2), extended light exposure during the diafiltration process should be avoided. The contribution of these photogenerated species is particularly evident in absorption at low dye concentrations, whereas in emission, it becomes prominent only at high dye concentrations, where fluorescence quenching of the dye is significant, as discussed below. Nonetheless, measurements performed several months after QS preparation, when a portion of the incorporated dye had photoreacted (as shown in Fig. S14), showed no significant decrease in fluorescence quantum yield. Moreover, the photogenerated species does not impact the intended application of these dye-loaded QSs as fluorescent probes for 2PM, since the new species is emissive in the far-red spectral region, which could, in principle, be exploited for imaging.

Importantly, dye **5**-loaded QS (Table 3) exhibited a fluorescence quantum yield (Φ_F) of 23% at the lowest dye loading, which is higher than that of the free dye in ethanol (17%, Table 3). This increase can be attributed to the more rigid environment provided by the QS membrane, which may reduce non-radiative relaxation pathways, or to partial protection from molecular oxygen, which can quench fluorescence. Upon increasing dye loading, the Φ_F decreased from 23% to 3%, highlighting the impact of aggregation on the emission efficiency and the dynamics of the incorporated dye. Fluorescence lifetimes (Table 3 and Fig. S14) indicate a modest increase upon entrapment in QSs, compared to ethanol and other organic solvents. This increase aligns with the high fluorescence quantum yield observed in QSs at lower dye concentrations. This phenomenon was already observed in previous dye-loaded QS formulations.[36] Notably, no substantial differences in lifetime were observed across varying dye loadings (Fig. S16), suggesting that the reduction in quantum yield at higher loadings can be attributed to the formation of non-emissive H-aggregates, which do not contribute to the overall fluorescence dynamics.

Despite reduced quantum yield at increased dye loadings, the estimated brightness per particle was still increased at higher loadings due to the significantly larger number of dye molecules per particle, yielding values of the order of 1×10^7 M^{-1} cm^{-1} (see Table 3), similar to ultrabright QS containing carbocyanine dyes.[36] This increase in brightness by 2–3 orders of magnitude with

Table 2 Physicochemical characterization of dye **5**-loaded quatsomes, at three dye loadings

	Q	Q-5-1	Q-5-7	Q-5-36
$[\text{Dye } 5]_{exp}$[a] (μM)	—	1.05 ± 0.06	7.2 ± 0.4	36 ± 2
$[\text{Membrane components}]_{exp}$[b] (mg mL^{-1})	1.2 ± 0.2	1.3 ± 0.2	1.4 ± 0.1	1.40 ± 0.02
Dye loading[c] (% w/w)	—	0.12 ± 0.02	0.76 ± 0.07	3.9 ± 0.2
d_{hyd}[d] (nm)	92.9 ± 0.6	116 ± 1	108 ± 2	142 ± 2
PDI	0.06 ± 0.01	0.02 ± 0.03	0.19 ± 0.04	0.22 ± 0.01
ζ-Potential[e] (mV)	10.1 ± 0.9	8 ± 2	8 ± 1	8 ± 2

[a] Calculated from absorbance values (Lambert–Beer Law). [b] Calculated from gravimetric analysis. [c] Loading = (mass dye)/(mass weighted-mass dye); where dye mass was obtained from absorbance (Lambert–Beer Law) and the total mass from gravimetric analysis. [d] Average d_{hyd} determined from DLS ± SD of three repeat measurements. [e] Average ζ-potential determined from ELS ± SD of three repeat measurements.

 This journal is © The Royal Society of Chemistry 2026

Open Access Article. Published on 11 February 2026. Downloaded on 2/25/2026 7:32:26 AM.
This article is licensed under a Creative Commons Attribution-NonCommercial 3.0 Unported Licence.

Table 3 Photophysical characterization of dye 5-loaded quatsomes

	λ_{max} abs[a] (nm)	λ_{max} emi[a] (nm)	$\Delta\lambda$[b] (cm^{-1})	τ[c] (ns)	Φ_F[d] (%)	Brightness one-photon[e] (M^{-1} cm^{-1})	Brightness per particle one-photon[f] (M^{-1} cm^{-1})	Brightness two-photon[g] (GM)	Brightness per particle two-photon[h] (GM)
Dye 5	603.5	632	28.5	0.792(1), 0.632(2), 0.588(3), 0.409(4)	17%(1), 13%(2), 12%(3), 6%(4)	3.7×10^4	—	340	—
Q-5-1	601	628	27	0.89	23%(5)	5×10^4	4.9×10^6	184	1.8×10^4
Q-5-7	602.5	628	25.5	0.87	8%(5)	1.7×10^4	1.2×10^7	48	3.4×10^4
Q-5-36	605.5	629	23.5	0.91	3%(5)	6.5×10^3	4.3×10^7	9	5.9×10^4

[a] Absorption and emission maxima. [b] Stokes shift. [c] Average fluorescence lifetimes. In the case of QS, a biexponential function has been employed to fit the experimental decays. Details of the fitting procedure are reported in Table S4. [d] Fluorescence quantum yield. [e] Brightness one-photon = $\phi_F \times \varepsilon$. [f] Brightness one-photon of a single fluorescent QS calculated as $\varepsilon_p \times \phi_F$, where ϕ_F is the fluorescence quantum yield and ε_p is the molar extinction coefficient at the maximum absorption wavelength (605 nm) of a single QS, calculated as $\varepsilon \times n$ (n is the estimated number of fluorophores per vesicle). [g] Brightness two-photon = $\phi_F \times \sigma_2$. [h] Brightness two-photon of a single fluorescent QS calculated as $\sigma_{2p} \times \phi_F$,[47] where ϕ_F is the fluorescence quantum yield and σ_{2p} is the two-photon cross section of a single QS at the maximum two-photon absorption wavelength (910 nm), calculated as $\sigma_2 \times n$ (n is the estimated number of fluorophores per vesicle (1) EtOH. (2) $CHCl_3$. (3) Toluene. (4) Cyclohexane. (5) PBS. Details in Tables S5–S7).

respect to the fluorophore in solution represents a crucial advantage for bioimaging applications, since the resulting improved signal-to-noise ratio yields better image quality and makes higher scanning speeds possible.[37]

Two-photon excitation spectra were collected for dye **5** and dye **5**-loaded quatsomes by exciting the samples over the 740–1300 nm spectral range. The quadratic dependence of the emitted fluorescence intensity on the excitation power was carefully verified (see the Materials and Methods section). The two-photon cross-section (σ_2) of dye **5**-loaded quatsomes (Q-**5**), which quantifies the probability of a two-photon absorption event and is expressed in Göppert-Mayer (GM) units,[48] showed values exceeding 300 GM for all three dye loadings (at the 910 nm peak) (Fig. 4H and Fig. S16), above those of common fluorophores effectively utilized in two-photon imaging, such as fluorescein and rhodamine B (around 18–40 GM).[49,50] σ_2 decreased with dye loading, from 800 GM at low dye loading, to 600 GM at intermediate loading, and 300 GM at high loading. The normalized TPA spectra of the nanovesicle dispersions (Fig. S17C) are independent of dye concentration and closely resemble the TPA bandshape of the free dye in ethanol but were slightly red-shifted. QS encapsulation preserves the very broad two-photon absorption range of the dye (750–1300 nm), a feature extremely advantageous for TPM, as it allows excitation across a wide spectral window. While σ_2 is lower than the free dye in ethanol (σ_2 = 2000 GM at the same wavelength), dye-loaded nanovesicles offer additional advantages, including their use in aqueous and therefore, biological media, and their higher 2P brightness. This makes them a valuable tool for two-photon microscopy, especially in *in vivo* and live-cell imaging, where factors such as excitation wavelength and long-term photostability are critical for obtaining high-quality images.[5,6,51]

Overall, the developed octupolar merocyanine based 2PM nanoprobes combine high brightness with strong and broad nonlinear optical properties in a highly stable nanoparticle, making them a promising tool for applications in two-photon absorption (2PA) microscopy.

4. Octupolar merocyanine dye-loaded quatsomes as two-photon microscopy probes in porcine scleral tissues

To assess the performance of the QSs as nanocarriers for hydrophobic fluorescent dyes in biologically relevant environments, we conducted *ex vivo* permeation experiments on isolated porcine sclera. This tissue, characterized by a dense matrix of collagen, proteoglycans and water-filled pores, provides a highly polar, cell-poor environment that serves as a useful preliminary model for evaluating the 2PM nanoprobe in aqueous biological conditions.[50,52] Scleral samples were treated for 2 hours with the aqueous dispersion of dye **5**-loaded QSs (QS-5-1), or a control solution of free dye **5** in water + 2.5% DMSO.

Upon excitation at 900 nm, the emission from dye **5** was detected in the red and far-red channels (604–679 nm and 698–750 nm, respectively) of the two-photon microscopy setup. Tissue structure and morphology were visualized *via* second harmonic generation (SHG) from collagen fibers,[53] which, under 900 nm excitation, falls within the blue detection channel (centered around 450 nm). Autofluorescence from the tissue was negligible under the experimental conditions employed, ensuring that the detected signal primarily originated from dye **5** and the SHG response. As shown in Fig. 5, tissues treated with the 2PM nanoprobes exhibited a markedly stronger red/far-red fluorescence signal at the surface compared to those treated

Open Access Article. Published on 11 February 2026. Downloaded on 2/25/2026 7:32:26 AM.
This article is licensed under a Creative Commons Attribution-NonCommercial 3.0 Unported Licence.

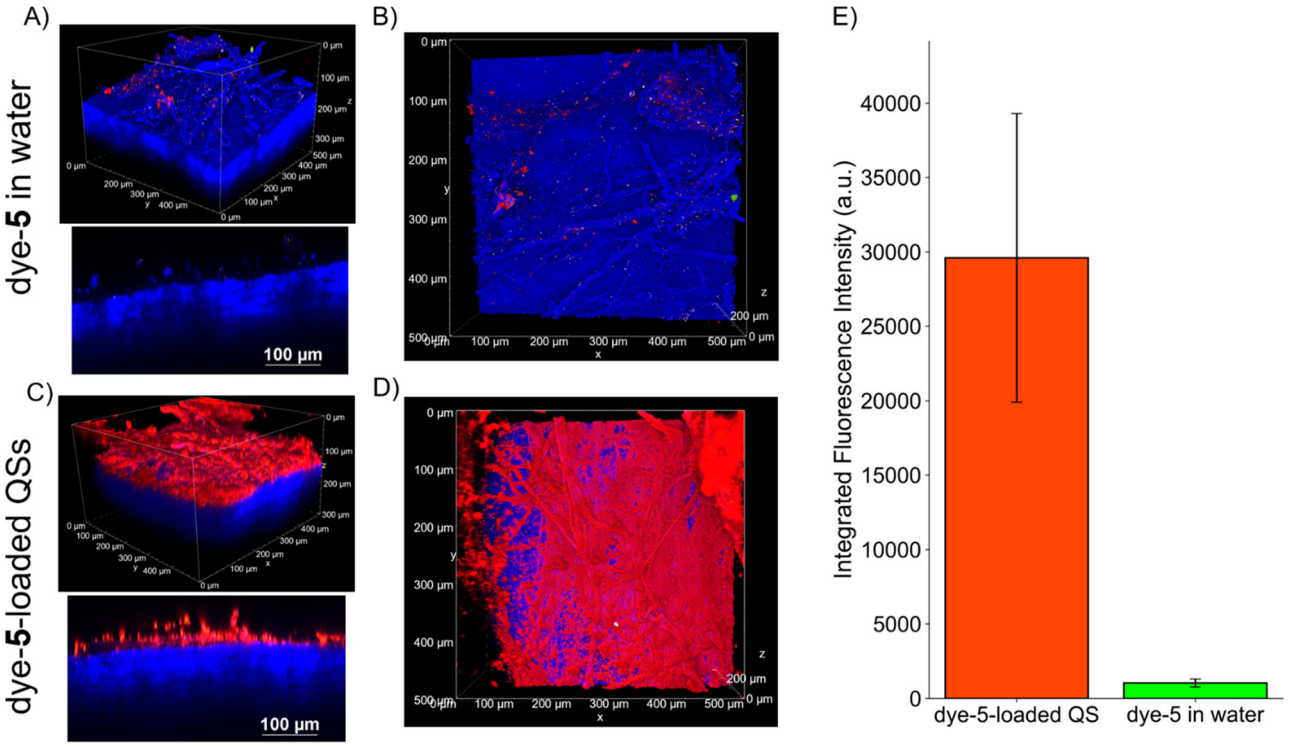

Fig. 5 Two-photon microscopy analysis of porcine scleral tissues after 2-hour exposure to dye **5**, either as a free solution in water (with 2.5% DMSO) or loaded in QSs. (A) and (B) 3D rendering, XZ, and XY views extracted from a Z-stack (step size: 2 µm; total depth: 300 µm) acquired on tissue treated with free dye **5** in aqueous solution. (C) and (D) 3D rendering, XZ, and XY views extracted from a Z-stack (step size: 2 µm; total depth: 300 µm) acquired on tissue treated with dye **5**-loaded QSs (dye concentration: 1 µM). (E) Bar plot of the integrated fluorescence intensities in the red channel (604–679 nm), averaged over the full depth of three Z-stacks acquired under identical conditions (excitation wavelength, laser power, detector gain) in distinct tissue regions for each sample. Error bars indicate the standard deviation across the three replicates for each treatment condition. All the images were acquired at an excitation wavelength of 900 nm.

with the free dye, which showed negligible emission (Fig. 5A and B). This result is consistent with the tendency of dye **5** to undergo aggregation and fluorescence quenching in aqueous environments. These effects are suppressed when the dye is loaded in the QS membrane, at least at low dye loading levels as QS-5-1. The enhanced surface fluorescence is quantified in the bar plot of Fig. 5E, which reports the average integrated signal from three independent Z-scans acquired under identical conditions in different regions of the sample. Despite this enhanced surface signal, no significant permeation of the dye into deeper layers of the tissue was observed. Emission spectra collected at two increasing depths (Fig. S18) revealed that the fluorescence from dye **5** rapidly diminished below the surface, becoming comparable to the intrinsic tissue autofluorescence after just 10–20 µm. The weak emission signal observed below the surface could be attributed to a limited penetration of the dye, which is strongly lipophilic, or to fluorescence quenching, as already observed in aqueous environments. For sure, the large size of the QSs hinders their diffusion into the small pores of the scleral matrix. Moreover, electrostatic interactions between the positively charged surfactant in the QS formulation and the negatively charged proteoglycans of the tissue may promote QS destabilization at the interface, further hindering the diffusion of the lipophilic dye.

To demonstrate the lipophilicity of dye **5**, experiments on porcine skin were carried out. The outer layer of the skin (the stratum corneum) is highly hydrophobic being constituted by death cells embedded in a lipid matrix. In these experiments, we did not observe any significant differences in fluorescence intensity between samples treated with QSs and those treated with the free dye (Fig. S19). This result confirms the strong lipophilicity of dye **5**, which contains long alkyl chains and readily partitions into the lipophilic outer layer of skin cells, regardless of the delivery system.

The 2PM results highlight the ability of QSs to preserve the emissive properties of hydrophobic dyes in aqueous biological environments, such as the sclera, thereby supporting their potential for bioimaging applications. Further investigations will include a systematic cytotoxicity assessment and the ability to undergo cellular internalization.[54]

5. Conclusions

We report the synthesis and spectroscopic characterization of four new merocyanine dyes designed for two-photon microscopy (2PM), characterized by varying numbers of hydrophobic (C18 alkyl) and hydrophilic (triethylene glycol) substituents. We

 This journal is © The Royal Society of Chemistry 2026

Open Access Article. Published on 11 February 2026. Downloaded on 2/25/2026 7:32:26 AM.
This article is licensed under a Creative Commons Attribution-NonCommercial 3.0 Unported Licence.

conducted a systematic screening of quatsome nanovesicle formulations incorporating these octupolar, red-emitting, merocyanine dyes. Stable incorporation of the dyes into the lipid quatsome bilayer required a minimum of two C18 alkyl chains per dye molecule, enabling the formation of highly fluorescent nanoprobes that maintained consistent size and emission properties over at least eight months. These optimal formulations exhibited two-photon absorption cross sections ranging from 300 to 800 GM at 910 nm and remarkable two-photon brightness per particle in the order of 1×10^4 GM, two orders of magnitude above that of the free dye. Two-photon microscopy experiments in porcine scleral tissue demonstrated the ability of these nanoprobes to retain the emissive properties of the hydrophobic merocyanine dyes in aqueous biological environments, underscoring their suitability for advanced bioimaging applications.

6. Materials and methods

6.1. Materials

All chemicals were used without any further purification. 5-Cholesten-3β-ol (CHOL, purity 95%) was purchased from PanReac (Castellar del Vallès, Spain). Myristalkonium chloride (MKC, purity > 98%) was supplied from TCI (Tokyo, Japan). Ethanol (EtOH, HPLC grade) was purchased from Teknokroma (Sant Cugat del Vallès, Spain). Phosphate buffered saline (PBS 100 mM) was prepared in our laboratory with 96 mM NaCl, 3 mM Na_2HPO_4, and 1 mM NaH_2PO_4. Carbon dioxide (purity ≥ 99.9%) was supplied by Carburos Metálicos S.A. (Barcelona, Spain). CHOL-PEG2000 was obtained from Creative PEGWorks (Chapel Hill, NC, USA).

6.2. Synthesis of merocyanine dyes 4–7

All reported ^{1}H and ^{13}C NMR spectra were collected using 500 MHz and 600 MHz spectrometers. Chemical shifts (δ ppm) were determined with TMS as the internal reference; *J* values are given in Hz. Chromatography was performed on silica gel (230–400 mesh) or aluminum oxide 90 active neutral (70–230 mesh). Size exclusion chromatography (SEC) was performed with Bio-Rad S-X1 Support in toluene.

6.2.1. 1,1-Dimethyl-2-methylene-3-octadecyl-2,3-dihydro-1*H*-benzo[*e*]indole, 2a. 1,1,2-Trimethyl-1*H*-benzo[*e*]indole 1.05 g (5.00 mmol) and 1-bromooctadecane 2.17 g (6.50 mmol) were heated in a pressure tube at 160 °C for 4 h. On cooling, 1.01 g (1.4 mL, 10 mmol) of triethylamine was added and mixed. The product was purified by column chromatography (silica, eluent : hexane-ethyl acetate 4 : 1), yield: 1.24 g (47%). ^{1}H NMR (500 MHz, $CDCl_3$) δ 7.94 (d, *J* = 8.6 Hz, 1H), 7.74 (d, *J* = 8.2 Hz, 1H), 7.67 (d, *J* = 8.6 Hz, 1H), 7.36 (dd, *J* = 8.4, 6.8 Hz, 1H), 7.16 (t, *J* = 8.2 Hz, 1H), 6.96 (d, *J* = 8.6 Hz, 1H), 3.92 (d, *J* = 9.9 Hz, 2H), 3.57 (t, *J* = 7.5 Hz, 2H), 1.70–1.62 (m, 8H), 1.41–1.31 (m, 4H), 1.31–1.20 (m, 28H), 0.88 (t, *J* = 6.8 Hz, 3H). ^{13}C NMR (126 MHz, $CDCl_3$) δ 163.6, 143.8, 130.2, 129.8, 129.1, 128.9, 126.8, 126.4, 121.6, 121.4, 109.0, 73.1, 46.3, 42.6, 32.1, 30.0, 29.9, 29.8, 29.8, 29.8, 29.7, 29.7, 29.6, 29.5, 27.4, 26.5, 22.9, 14.3. HRMS (ESI) calcd for $C_{33}H_{52}N$ 462.4100 $[MH]^+$, found 462.4099 (Fig. S20).

6.2.2. 3-(2-(2-(2-Methoxyethoxy)ethoxy)ethyl)-1,1-dimethyl-2-methylene-2,3-dihydro-1*H*-benzo[*e*]indole, 2b. Obtained analogously to **2a**. The product was purified by column chromatography (silica, eluent: CH_2Cl_2–CH_3OH 97 : 3. Yield: 42%.

^{1}H NMR (500 MHz, $CDCl_3$) δ 7.94 (d, *J* = 8.7 Hz, 1H), 7.74 (d, *J* = 8.3 Hz, 1H), 7.66 (d, *J* = 8.6 Hz, 1H), 7.37 (ddd, *J* = 8.5, 6.7, 1.3 Hz, 1H), 7.17 (ddd, *J* = 8.0, 6.7, 1.1 Hz, 1H), 7.08 (d, *J* = 8.7 Hz, 1H), 3.95 (br. s, 2H), 3.82 (t, *J* = 6.3 Hz, 2H), 3.71 (t, *J* = 6.3 Hz, 2H), 3.64–3.54 (m, 6H), 3.48–3.43 (m, 2H), 3.33 (s, 3H), 1.65 (s, 6H). ^{13}C NMR (126 MHz, $CDCl_3$) δ 163.5, 143.8, 130.1, 129.7, 129.1, 129.0, 126.6, 126.4, 121.6, 121.6, 109.5, 77.4, 77.2, 76.9, 73.5, 72.0, 71.1, 70.8, 70.7, 67.5, 59.1, 46.3, 42.9, 30.0. HRMS (ESI) calcd for $C_{22}H_{30}NO_3$ 356.2226 $[MH]^+$, found 356.2227 (Fig. S21).

6.2.3. (3*E*,5*E*)-3,5-Bis((*Z*)-2-(1,1-dimethyl-3-octadecyl-1,3-dihydro-2H-benzo[*e*]indol-2-ylidene)ethylidene)-2-hydroxy-4,6-dioxocyclohex-1-ene-1-carbaldehyde, 3a. A mixture of compound **2a** 0.5 g (1.08 mmol) and 2,4,6-trihydroxybenzene-1,3,5-tricarbaldehyde 0.105 g (0.5 mmol) in toluene (5 mL) was heated at 110 °C for 2 h. On cooling, the solvent was evaporated and the residue was eluted through a silica column with a CH_2Cl_2–CH_3OH (96 : 4) mixture to give 0.07 g (9%) of crude compound **4** and 0.33 g of pure compound **3a** (yield 60%).

^{1}H NMR (600 MHz, $CDCl_3$) δ 9.95 (s, 1H), 8.98 (d, *J* = 14.3 Hz, 2H), 8.94 (br.s, 2H), 8.20–8.13 (m, 3H), 7.95–7.87 (m, 4H), 7.62 (ddd, *J* = 8.3, 6.8, 1.3 Hz, 1H), 7.58 (ddd, *J* = 8.4, 6.7, 1.3 Hz, 1H), 7.47 (ddd, *J* = 8.0, 6.7, 1.1 Hz, 1H), 7.43 (t, *J* = 7.2 Hz, 1H), 7.33 (d, *J* = 8.8 Hz, 1H), 7.29 (d, *J* = 8.7 Hz, 1H), 4.18–4.08 (m, 4H), 2.09 (2.17–2.02 (m, 12H), 1.92 (dt, *J* = 15.2, 7.5 Hz, 4H), 1.54–1.47 (m, 4H), 1.45–1.37 (m, 4H), 1.35–1.18 (m, 52H), 0.87 (t, *J* = 7.0 Hz, 6H). ^{13}C NMR (151 MHz, $CDCl_3$) δ 140.0, 139.7, 134.1, 131.8, 131.5, 130.4, 130.1, 130.1, 128.6, 128.4, 127.8, 127.6, 125.0, 124.5, 122.3, 110.4, 110.4, 51.2, 50.9, 44.6, 44.3, 32.1, 29.8, 29.8, 29.7, 29.7, 29.7, 29.5, 29.4, 28.9, 28.7, 27.5, 27.4, 27.2, 27.2, 22.8, 14.3. HRMS (APCI) calcd for $C_{75}H_{105}N_2O_4$ 1097.8074 $[MH]^+$, found 1097.8077 (Fig. S22).

6.2.4. (3*E*,5*E*)-2-Hydroxy-3,5-bis((*Z*)-2-(3-(2-(2-(2-methoxyethoxy)-ethoxy)ethyl)-1,1-dimethyl-1,3-dihydro-2H-benzo[*e*]indol-2-ylidene)-ethylidene)-4,6-dioxocyclohex-1-ene-1-carbaldehyde, 3b. The synthetic procedure is analogous to compound **3a**. On cooling, the solvent was evaporated, crude compound **3b** was used for the second step.

HRMS (APCI) calcd for $C_{53}H_{61}N_2O_{10}$ 885.4323 $[MH]^+$, found 885.4329.

6.2.5. (2*Z*,4*Z*,6*E*)-2-((*E*)-2-(1,1-Dimethyl-3-octadecyl-1,3-dihydro-2*H*-benzo[*e*]indol-2-ylidene)ethylidene)-4,6-bis((*Z*)-2-(1,1-dimethyl-3-octadecyl-1,3-dihydro-2*H*-benzo[*e*]indol-2-ylidene)ethylidene)cyclohexane-1,3,5-trione, 4. A mixture of compound **2a** 0.46 g (1 mmol) and 2,4,6-trihydroxybenzene-1,3,5-tricarbaldehyde 0.052 g (0.25 mmol) in pirydine (1 mL) was heated at 140 °C for 2 h. On cooling, the solvent was evaporated. To remove intermediate products the mixture was eluted through a short alumina column of 5–7 cm (*d* = 4 cm) with a hexane–ethyl acetate (9 : 1) mixture. Solvents were evaporated and residue was eluted through z silica column with a hexane–ethyl acetate (3 : 1) mixture. Solvents were evaporated and the residue was dried in a vacuum. Yield: 0.29 g

Open Access Article. Published on 11 February 2026. Downloaded on 2/25/2026 7:32:26 AM. This article is licensed under a Creative Commons Attribution-NonCommercial 3.0 Unported Licence.

(75%). The ^{1}H NMR spectrum shows broadened signals due to the presence of equilibrium between rotamers. The ^{1}H NMR spectrum of the same sample measured at 40 °C is better resolved, though some signals are somewhat broadened. ^{1}H NMR (500 MHz, $CDCl_3$) δ 8.95 (br.s, 3H), 8.25–8.09 (ma, 6H), 7.93–7.81 (m, 6H), 7.55 (t, J = 7.7 Hz, 3H), 7.38 (t, J = 7.5 Hz, 3H), 7.25 (d, J = 9.6 Hz, 3H), 4.09 (br.s, 6H), 2.12 (s, 18H), 1.94 (quint, J = 7.7 Hz, 6H), 1.58–1.49 (m, 6H), 1.48–1.40 (m, 6H), 1.34–1.16 (m, 78H), 0.87 (t, J = 7.1 Hz, 12H). ^{1}H NMR (500 MHz, $CDCl_3$, 40 °C) δ 8.94 (d, J = 13.6 Hz, 3H), 8.22–8.11 (m, 6H), 7.91–7.81 (m, 6H), 7.55 (t, J = 7.6 Hz, 3H), 7.38 (t, J = 7.5 Hz, 3H), 7.24 (d, J = 8.7 Hz, 3H), 4.09 (t, J = 7.5 Hz, 6H), 2.12 (s, 18H), 1.95 (quint, J = 7.6 Hz, 6H), 1.54 (quint, J = 7.8 Hz, 6H), 1.45 (quint, J = 7.7 Hz, 6H), 1.33–1.21 (m, 78H), 0.87 (t, J = 7.0 Hz, 12H). ^{13}C NMR (126 MHz, $CDCl_3$) δ 146.9, 140.6, 131.0, 130.0, 129.9, 128.8, 127.3, 122.3, 110.2, 77.4, 77.2, 76.9, 50.3, 43.9, 32.1, 29.9, 29.8, 29.8, 29.6, 29.5, 28.9, 27.4, 27.3, 22.8, 14.3. HRMS (APCI) calcd for $C_{108}H_{154}N_3O_3$ 1541.1990 $[MH]^+$, found 1541.1998 (Fig. S23 and S24).

Mixed synthesis of compounds **4**, **5** and **6** from compounds **2a** and **3b**.

A mixture of compounds **2a** 0.31 g (0.28 mmol) and **3b** 0.15 g (0.42 mmol) in 4 mL of pyridine was heated at 140 °C for 3h. The solvent was evaporated and the residue was eluted through an alumina column with a CH_2Cl_2–MeOH 99 : 1 mixture (intermediate products removal). After solvent evaporation, the residue was eluted through a silica column with CH_2Cl_2–MeOH 97 : 3 resulting in three fractions 1: compound **4** (40 mg, 9%), 2: compound **5** (85 mg, 21%) and 3: compound **6** (60 mg, 16%)

6.2.6. (2*Z*,4*Z*,6*E*)-2-((*E*)-2-(1,1-Dimethyl-3-octadecyl-1,3-dihydro-2*H*-benzo[*e*]indol-2-ylidene)ethylidene)-4-((*Z*)-2-(1,1-dimethyl-3-octadecyl-1,3-dihydro-2*H*-benzo[*e*]indol-2-ylidene)ethylidene)-6-((*Z*)-2-(3-(2-(2-(2-methoxyethoxy)ethoxy)ethyl)-1,1-dimethyl-1,3-dihydro-2*H*-benzo[*e*]indol-2-ylidene)ethylidene)cyclohexane-1,3,5-trione, 5. ^{1}H NMR (500 MHz, CD_2Cl_2) δ 8.95–8.73 (m, 3H), 8.22–8.02 (m, 6H), 7.90 (t, J = 9.7 Hz, 6H), 7.57 (br.s, 3H), 7.47–7.28 (m, 6H), 4.31 (br.s, 2H), 4.09 (br.s, 4H), 4.01 (br.s, 2H), 3.70–3.62 (m, 2H), 3.58–3.43 (m, 4H), 3.40–3.32 (m, 2H), 3.29–3.20 (m, 3H), 2.10 (s, 18H), 1.95 (t, J = 7.6 Hz, 4H), 1.56 (quint, J = 7.7 Hz, 4H), 1.51–1.44 (m, 4H), 1.44–1.03 (m, 52H), 0.87 (t, J = 6.8 Hz, 6H). ^{13}C NMR (126 MHz, CD_2Cl_2) δ 188.9, 188.8, 186.3, 184.7, 175.8, 175.6, 175.1, 174.8, 174.3, 147.5, 147.2, 146.6, 141.2, 133.0, 132.7, 132.4, 131.6, 131.5, 131.4, 130.4, 130.3, 130.1, 130.0, 129.2, 129.0, 127.7, 127.7, 124.3, 124.1, 122.6, 119.4, 111.7, 110.8, 110.7, 99.3, 98.9, 72.4, 71.8, 71.0, 68.4, 68.3, 59.1, 50.6, 50.4, 44.6, 44.3, 32.5, 30.3, 30.2, 30.1, 30.0, 29.9, 29.1, 27.9, 27.8, 27.7, 27.6, 23.3, 14.5. HRMS (APCI) calcd for $C_{97}H_{132}N_3O_6$ 1435.0116 $[MH]^+$, found 1435.0117 (Fig. S25 and S26).

6.2.7. (2*Z*,4*Z*,6*E*)-2-((*E*)-2-(1,1-dimethyl-3-octadecyl-1,3-dihydro-2*H*-benzo[*e*]indol-2-ylidene)ethylidene)-4,6-bis((*Z*)-2-(3-(2-(2-(2-methoxyethoxy)ethoxy)ethyl)-1,1-dimethyl-1,3-dihydro-2*H*-benzo[*e*]indol-2-ylidene)ethylidene)cyclohexane-1,3,5-trione, 6. ^{1}H NMR (500 MHz, $CDCl_3$) δ 8.94 (br.s, 3H), 8.20–8.02 (m, 6H), 7.92–7.78 (m, 6H), 7.59–7.51 (m, 3H), 7.48–7.31 (m, 6H), 4.32 (br.s, 4H), 4.12–4.07 (m, 2H), 4.00 (br.s, 4H), 3.66 (br.s, 4H), 3.56 (br.s, 4H), 3.51 (br.s, 4H), 3.39 (br.s, 4H), 3.28 (s, 6H), 2.12 (s, 18H), 1.93 (br.s, 2H), 1.53 (br.s, 2H), 1.43 (br.s, 2H), 1.32–1.16 (m, 26H), 0.86 (t, J = 6.9 Hz, 3H). ^{13}C NMR (126 MHz, $CDCl_3$) δ 185.3, 175.1, 146.6, 141.2, 140.5, 133.0, 132.3, 131.1, 130.0, 129.6, 128.7, 128.6, 127.4, 127.2, 124.0, 123.8, 122.2, 111.2, 110.2, 99.0, 72.0, 71.3, 70.7, 68.1, 59.1, 50.4, 50.2, 44.1, 43.9, 32.0, 29.8, 29.8, 29.6, 29.5, 28.9, 27.3, 27.3, 22.8, 14.3. HRMS (APCI) calcd for $C_{86}H_{110}N_3O_9$ 1328.8242 $[MH]^+$, found 1328.8224 (Fig. S27 and S28).

Mixed synthesis of compounds **4**, **5** and **6** from compounds **2b** and **3a**.

A mixture of compounds **2b** 0.56 g (0.63 mmol) and **3a** 0.32 g (0.69 mmol) in 4 mL of pyridine was heated at 140 °C for 2h. On cooling the solvent was evaporated. The crude mixture was passed through a short alumina column of 5–7 cm (d = 4 cm) in a CH_2Cl_2–CH_3OH (98.5 : 1.5) mixture. After evaporation, the residue was eluted through a silica column with CH_2Cl_2–CH_3OH (96 : 4) to give three fractions; 1: compound **4** (20 mg, 2%), 2: compound **5** (150 mg, 17%), and fraction 3 contained two dye products (440 mg).

Dye products from the last fraction were separated by column chromatography through silica with an ethyl acetate–CH_3OH (98 : 2) mixture which gives rise to compound **6** (180 mg, 22%). The CH_3OH ratio in the eluent system was then increased to ethyl acetate–CH_3OH 95 : 5 which allowed the elution of compound **7** (75 mg, 10%).

6.2.8. (2*Z*,4*Z*,6*E*)-2-((*E*)-2-(3-(2-(2-(2-Methoxyethoxy)ethoxy)ethyl)-1,1-dimethyl-1,3-dihydro-2*H*-benzo[*e*]indol-2-ylidene)ethylidene)-4,6-bis((*Z*)-2-(3-(2-(2-(2-methoxyethoxy)ethoxy)ethyl)-1,1-dimethyl-1,3-dihydro-2*H*-benzo[*e*]indol-2-ylidene)ethylidene)cyclohexane-1,3,5-trione, 7. ^{1}H NMR (600 MHz, $CDCl_3$) δ 9.01–8.83 (m, 3H), 8.16–7.99 (m, 6H), 7.87 (d, J = 8.2 Hz, 3H), 7.82 (d, J = 8.7 Hz, 3H), 7.54 (t, J = 7.6 Hz, 3H), 7.41 (d, J = 8.8 Hz, 3H), 7.37 (t, J = 7.4 Hz, 3H), 4.31 (br.s, 6H), 3.98 (br.s, 6H), 3.65 (br.s, 6H), 3.60–3.46 (m, 12H), 3.38 (br.s, 6H), 3.28 (s, 9H), 2.11 (s, 18H). ^{13}C NMR (151 MHz, $CDCl_3$) δ 186.5, 175.6, 175.0, 147.6, 146.8, 146.1, 141.1, 132.3, 131.1, 130.0, 129.6, 128.5, 127.3, 127.2, 123.8, 122.2, 111.2, 99.2, 98.7, 72.0, 71.3, 70.7, 70.7, 68.1, 59.1, 50.3, 44.1, 32.1, 29.8, 29.8, 29.5, 29.3, 28.9, 22.8, 14.3. Due to equilibrium between rotamers chemical shifts of weakly intensive signals in the ^{13}C NMR spectrum were determined by the HSQC technique. HRMS (APCI) calcd for $C_{75}H_{88}N_3O_{12}$ 1222.6368 $[MH]^+$, found 1222.6393 (Figure S29, S30, S31).

6.3. Production of dye-loaded CHOL/MKC QS by DELOS-SUSP

Quatsomes are synthesized using the depressurization of an expanded liquid organic solution-suspension (DELOS-SUSP) methodology, which is a one-step green robust scalable process based on compressed fluids technologies.[41,42] This method consists of the depressurization of a CO_2-expanded organic liquid solution into an aqueous phase using mild conditions of temperature (308 K) and pressure (10 MPa). For its preparation (Table S2), 27 mg of cholesterol, 26.5 mg of MKC and the corresponding mg of dye (0.083 mg, 0.413 mg and 2.06 mg for the lower, medium and high concentration respectively) were added to 2.304 mL of ethanol. Finally, 5.16 mg of CHOL-PEG2000 were added to 0.576 mL of DMSO, and it was mixed

 This journal is © The Royal Society of Chemistry 2026

Open Access Article. Published on 11 February 2026. Downloaded on 2/25/2026 7:32:26 AM.
This article is licensed under a Creative Commons Attribution-NonCommercial 3.0 Unported Licence.

together with the ethanol solution. The solution was loaded into a 7.5 mL high-pressure reactor. Then, compressed CO_2 was added, reaching one-phase in the reactor containing the above components. After 1 h, the solution was depressurized over 25.92 mL of PBS 100 mM. The resulting suspension had a total concentration of QSs of approximately 2.05–2.10 mg mL^{-1}, depending on the dye concentration.

To remove the ethanol and the residual membrane components in the QS membrane, one step of purification was applied. In this study, we purified the nanovesicles by diafiltration, using the KrosFlo Diafiltration equipment, from Spectrum Labs. In our case, we used a size-exclusion column of 100 kDa and a surface area of 20 cm^2 (MicroKros, Spectrum Labs). All of the quatsomes were diafiltered in PBS 100 mM, applying six cycles of recircularization at a feed flow rate of 15 mL min^{-1} and a transmembrane pressure of about 5 psi.

6.4. Determination of membrane component concentration

For the determination of membrane component concentration, QSs were freeze-dried (LyoQuest-80, Telstar) at 193 K and 5 Pa for 5 days. A volume (V_{vial}) of 1 ml of the sample was placed in a 4 mL glass vial and covered with a holey aluminium foil to let the sublimated solvents escape. Triplicates of each sample were performed to obtain more reliable measurements. All vials were weighed before and after the process, so the residue mass is obtained. Then, the quatsome concentration can be computed by:

$$[\text{membrane components}]_{exp} = \text{residue mass}/V_{vial}$$

6.5. Determination of dye concentration in dye-loaded QSs

To determine the concentration and mass of dye entrapped in the QSs, the UV-Vis absorbance of each dye was measured using a UV-Vis spectrophotometer (Varian Cary 5, Agilent). The QS membrane was dissociated by diluting the samples in ethanol until a value of absorption unit of 0.1–0.3 is obtained. The concentration of each dye was determined using the Lambert–Beer law (Abs = $c \times \varepsilon \times l$), where c is the concentration (M), ε is the molar extinction coefficient (M^{-1} cm^{-1}), and l is the path length (cm), using a high precision cell (Hellma Analytics) of 1 cm, as a cuvette. The molar extinction coefficients used are: $\varepsilon_{580\,nm}^{Dye\,4}$, EtOH = 220 000 M^{-1} cm^{-1}, $\varepsilon_{580\,nm}^{Dye\,5}$, EtOH = 218 000 M^{-1} cm^{-1}, $\varepsilon_{580\,nm}^{Dye\,6}$, EtOH = 219 000 M^{-1} cm^{-1} and $\varepsilon_{580\,nm}^{Dye\,7}$, EtOH = 217 000 M^{-1} cm^{-1}.

For the determination of the dye loading, the concentration of membrane components, determined after lyophilization (explained above), was used and the loading in mass was determined through:

$$\text{Dye loading} = \text{mass dye}_{exp}/(\text{mass MC}_{exp} - \text{mass dye})$$

MC = membrane components

6.6. Physicochemical characterization of dye-loaded QS

6.6.1. Dynamic light scattering (DLS) and electrophoretic light scattering (ELS). The hydrodynamic diameter and the dispersity ($Đ$) were determined with the Zetasizer Ultra, from Malvern Instruments (Malvern, UK), using an incident light with a wavelength of 633 nm and measuring the scattered light at 173° with homodyne detection. The measurements were done with a dilution 1/10 in PBS 100 mM at 25 °C. Three different experiments were performed in order to check the reproducibility of the results. Results are given in percentage of the scattered light intensity, obtained by the cumulants method (Z-average). For the ζ-potential measurements the same equipment was used but measuring the dispersion light at 13°. The cuvette used is a DTS1070 folded capillary cell, from Malvern Instruments, applying a voltage of 20 mV between the electrodes. The measurements were performed with a dilution 1/10 in PBS 100 mM and the Smoluchowski equation was employed.

6.6.2. Cryogenic transmission electron microscopy. Cryogenic transmission electronic microscopy (cryo-TEM) images were acquired with a JEOL JEM microscope (JEOL JEM 2011, Tokyo, Japan) operating at 200 kV under low-dose conditions. The sample was deposited onto the holey carbon grid and then was immediately vitrified by rapid immersion in liquid ethane. The vitrified sample was mounted onto a cryo-transfer system (Gatan 626) and introduced into the microscope. Images were recorded on a CCD camera (Gatan Ultrascan US1000) and analyzed with the Digital Micrograph 1.8 software.

6.7. Spectroscopy characterization of free dye and dye-loaded QSs

6.7.1. UV-Vis spectroscopy. Solutions for spectroscopic measurements were prepared using spectroscopic or HPLC-grade solvents. Absorption spectra were measured with a UV-Vis-NIR spectrophotometer (Varian Cary 5000, Agilent Technologies, USA). Optical data analysis and the control of optional accessories were made with the modular Cary WinUV software. The measurement parameters were from 800 nm to 300 nm of wavelength. Samples were placed in a quartz high precision cell (Hellma Analytics, Germany). The absorption spectra were corrected to account for scattering contributions by subtracting the scattering profile recorded from a suspension of blank QSs, which was adjusted (by subtracting a constant value and scaling by a constant factor) for each absorption spectrum to be corrected (Fig. S32).

UV-Vis absorption measurements for the solvatochromism study of the four dyes and fluorescence quantum yield estimation were performed with a PerkinElmer Lambda650 spectrophotometer. In the case of QS dispersions, absorbance values were corrected to account for scattering contributions as explained above (Fig. S32).

6.7.2. Fluorescence spectroscopy. Emission spectra reported for Fig. 3 and for the stability study over time (Fig. 4G and Fig. S6) were recorded with a Fluorimeter Agilent Varian Cary Eclipse. Samples were excited at 570 nm and emission was recorded from 580 to 800 nm, with excitation and emission slits set at 10 nm.

Emission spectra, excitation spectra and fluorescence lifetime decays were recorded with a FLS1000 Edinburgh fluorometer using appropriate long-pass filters to suppress scattered excitation light. Fluorescence quantum yields of all the samples were measured using fluorescein in NaOH aq 0.1 M as the

Open Access Article. Published on 11 February 2026. Downloaded on 2/25/2026 7:32:26 AM. This article is licensed under a Creative Commons Attribution-NonCommercial 3.0 Unported Licence.

standard (ϕ = 0.9) and accounting for the scattering contributions in the case of QS dispersions by using absorbance values corrected by subtracting the scattering profile of a blank QS suspension.

Lifetime decays were acquired by exciting samples with a pulsed diode laser (~200 ps pulse duration and 405 nm as excitation wavelength) at a repetition rate of 1 MHz.

6.8. DFT and TD-DFT calculations on transoid and cisoid isomers

DFT geometry optimizations were carried out using the CAM-B3LYP functional and the 6-31G(d,p) basis set in the gas phase using Gaussian16, Revision B.01.[55] To reduce computational costs, in Fig. S11 we initially modeled a simplified structure containing a single chromophoric arm, replacing the long alkyl/triethylene glycol chains with butyl groups. This simplification is justified by experimental evidence showing that dyes **4–7** exhibit analogous absorption and emission spectra, indicating that peripheral chains have only a marginal influence on the optical properties of the chromophoric core. Both transoid (panel a) and cisoid (panel d) isomers were considered, the latter obtained by twisting the arm from the transoid geometry to simulate the experimentally proposed *cis–trans* photoisomerization process underlying the observed red-shifted absorption at 700 nm. For each isomer, ground-state geometry optimizations were followed by time-dependent DFT (TD-DFT) calculations at the same level of theory.

6.9. Two-photon absorption spectra and cross section

Two-photon absorption cross sections were obtained by comparing the two-photon excited fluorescence (TPEF) intensity collected from the samples to that of a reference, a solution of fluorescein in water at pH > 10 (0.1 M NaOH), following a procedure described in the literature.[45,48] The experimental setup consists of a Nikon A1R MP+ multiphoton upright microscope equipped with a Coherent Chameleon Discovery femtosecond pulsed laser (~100 fs pulse duration with 80 MHz repetition rate, tunable excitation range 700–1300 nm). A 25× water dipping objective (Nikon CFI APO LWD) with a numerical aperture of 1.1 and 2 mm working distance was employed for focusing the excitation beam and for collecting the TPEF. The TPEF signal was directed by a dichroic mirror to a high sensitivity photomultiplier GaAsP detector, connected to the microscope through an optical fiber and preceded by a dispersive element. This detector allowed the spectral profile of the TPEF signal (wavelength range 430 to 650 nm with a bandwidth of 10 nm) to be recorded. The emission spectra were always corrected for the wavelength dependent sensitivity of the detector. The measurements were carried out using 1 cm quartz cells placed horizontally under the microscope objective. Distilled water was employed to dip the objective, and the focal point was moved as close as possible to the upper cuvette wall, at the same exact height for the reference and the samples.

The concentration of dye **5** in EtOH used for estimating the σ_2 was 2 μM. The fluorescein solutions used as the reference were prepared with a concentration between 14 and 18 μM.

The corrected emission spectra obtained by one- and two-photon excitation were well superimposed for all the investigated solutions within the wavelength range available at the microscope (Fig. S33), confirming that the emitting state is the same for both processes. Therefore, for each sample and for the reference, we assumed the same fluorescence quantum yield for one- and two-photon excited fluorescence.

Following the procedure reported in the literature, the two photon absorption (TPA) cross section of the sample σ_2 as a function of the excitation wavelength, can be obtained as:[48]

$$\sigma_2(\lambda) = S\frac{\phi_{\mathrm{ref}}}{\phi}\frac{C_{\mathrm{ref}}}{C}\frac{P(\lambda)_{\mathrm{ref}}^2}{P(\lambda)^2}\frac{F(\lambda)}{F(\lambda)_{\mathrm{ref}}}\frac{n_{\mathrm{ref}}}{n}\sigma_{2,\mathrm{ref}}(\lambda)$$

where σ_2, ref is the TPA cross section of the reference, ϕ is the fluorophore quantum yield, C is the solution concentration, n is the refractive index, $P(\lambda)$ is the laser power at wavelength λ, and $F(\lambda)$ is the integral of the TPEF spectrum, evaluated after correcting the emission spectrum for the detector sensitivity. The subscript ref is associated with the reference properties, while the other terms refer to the sample. Since only a portion of the dye **5** emission spectrum falls within the spectral detector's sensitivity range, a multiplicative scale factor (S) was determined to account for the missing spectral region. This factor was estimated by calculating the ratio between the emission spectrum recorded with an Edinburgh fluorimeter (using the emission bandshape of the Q-5-1 suspension) and the corresponding spectrum obtained using the two-photon microscope (Fig. S33).

For each excitation wavelength, the quadratic dependence of the signal on excitation power was verified for all solutions. The log–log power dependence of the emission signal at 1100 nm is reported in Fig. S34. The maximum deviation did not exceed 30% for wavelengths above 920 nm. In contrast, for wavelengths below 920 nm, larger deviations from quadraticity indicate a non-negligible contribution from linear absorption.

The absolute values of $\sigma_{2,\mathrm{ref}}(\lambda)$ of fluorescein were taken from the literature.[56] TPA cross sections are expressed in Goeppert-Mayer units: 1 GM = 10–50 cm^4 s $photon^{-1}$.

6.10. Colloidal and optical stability of dye-loaded QSs

The stability of dye-loaded QSs over time was evaluated by measuring the changes of hydrodynamic diameter and dispersity, and the evolution of the maximum in absorbance and emission spectra. Changes were followed for two weeks, four, twelve, and thirty-three weeks after sample production (Fig. 4C, G and Fig. S6).

6.11. *Ex vivo* evaluation: two-photon microscopy

Ex vivo experiments were performed using fresh porcine sclera, isolated from pig eyes, and skin samples, collected from the pig ears and stored at −20 °C for no more than three months. Porcine tissues from both female and male animals (Landrace and Large White breeds; 10–11 months of age; 145–190 kg) were provided by a local abattoir (Macello Annoni S.p.A., Busseto, Italy). Both tissue types were treated following the same protocol: they were placed in Franz-type diffusion cells and incubated for 2 hours at room temperature with the formulation under study (QS-5-1 or dye 5 in water). Then, the formulation was removed, and tissue surface was carefully washed using saline

 This journal is © The Royal Society of Chemistry 2026

Open Access Article. Published on 11 February 2026. Downloaded on 2/25/2026 7:32:26 AM.
This article is licensed under a Creative Commons Attribution-NonCommercial 3.0 Unported Licence.

solution. Tissue discs, corresponding to the contact area, were punched and mounted in a custom plexiglass holder, soaked in saline solution to prevent dehydration and finally analyzed with the same Nikon A1R MP+ Upright Two-Photon Microscope previously used for the two-photon absorption measurements. The objective was dipped directly into the saline solution during image acquisition. Two-photon excited fluorescence (TPEF) and second harmonic generation (SHG) signals were collected using a dichroic mirror and directed to four non-descanned GaAsP photomultiplier tubes (PMTs), each preceded by optical filters for the simultaneous detection of four spectral windows: blue (415–485 nm), green (506–593 nm), red (604–679 nm), and far-red (698–750 nm). Image overlay and processing were performed using the microscope's dedicated software. Additionally, the GaAsP-based spectral detector described in Section 4 was used to acquire emission spectra directly from tissue samples. Images were acquired at excitation wavelengths of 900 or 1080 nm, with a typical field of view of 500 μm × 500 μm. In the case of the scleral tissue, three different tissue regions of each sample were analyzed, and Z-stacks were acquired under identical experimental conditions to allow for direct comparison between samples and evaluation of fluorescence signal distribution and intensity.

The reference suspension of dye **5** in water (with 2.5% DMSO) was obtained by dissolving the dye in DMSO to achieve a concentration of 40 μM. An aliquot of the DMSO stock solution was diluted in distilled water to reach a final DMSO content of 2.5% v/v (*i.e.*, 62.5 μL of stock solution in a total volume of 2500 μL). The resulting final concentration of dye **5** was approximately 1 μM, matching the concentration used in the QS suspensions.

Author contributions

Conceptualization: SGR, YMP, AD, NV, CS, DTG, MK. Methodology: SGR, YMP, AD, SP, GVN, JMF, OR, FDM, NV, CS, DTG, MK. Formal analysis: SGR, YMP, AD, OR, FDM. Investigation: SGR, YMP, AD. Data curation: SGR, YMP, AD. Writing – original draft: SGR, YMP, AD. Writing – review & editing: SP, GVN, JMF, OR, FDM, NV, CS, DTG, MK. Resources: SP, NV, CS, DTG, MK. Funding acquisition: SP, NV, CS, DTG, MK. Supervision: NV, CS, DTG, MK. Project administration: NV, CS, DTG, MK.

Conflicts of interest

The following authors declare the following financial interests/personal relationships which may be considered as potential competing interests: N. V. is the inventor of the patent WO2006079889, which protects the DELOS-SUSP methodology, owned by Nanomol Technologies SL.

Data availability

The data that support the findings of this study are available in the supplementary information (SI) of this article. Supplementary information: supporting figures and tables with additional experimental details, characterization data, and details regarding the DFT and TD-DFT calculations. See DOI: https://doi.org/10.1039/d5tb02465j.

Additional data are available on request from the corresponding authors.

Acknowledgements

This work has received funding from the European Union's Horizon 2020 research and innovation programme under the Marie Skłodowska-Curie grant agreement No. 101007804-Micro4Nano, and was further financially supported by the Generalitat de Catalunya (2021 SGR 00438 and 2024 PROD 00075), the Spanish Ministry for Science and Innovation (PID2022-137332OB-I00), the Severo Ochoa Program for Centers of Excellence in R&D (CEX2019-000917-S and CEX2023-001263-S), the Polish National Science Centre (OPUS 2020/37/B/ST4/00017), the Italian National Recovery and Resilience Plan (NRRP) funded by the European Union – NextGenerationEU (P2022ALSMP), and the Spanish Institute of Health Carlos III through the CIBER group CB06/01/0033. The research benefited from the COMP-R Initiative, funded by the 'Departments of Excellence' program of the Italian Ministry for University and Research (MUR, 2023–2027) and the HPC (High Performance Computing) facility of the University of Parma, Italy. SG was funded by an FPI fellowship (PRE2022-101359) linked to the Severo Ochoa program (CEX2019-000917-S) at ICMAB-CSIC, OR was funded by the PNRR MUR project ECS-00000033-ECOSISTER, and AD was funded by PNRR MUR project BIOCOMMON – project number 2022A58EE5. This work was carried out within the framework of the PhD Programme in Biochemistry, Molecular Biology and Biomedicine at the Universitat Autònoma de Barcelona. The 2PA nanoprobes were prepared and characterized at the ICTS NANBIOSIS unit 6 (Soft Materials Service) located at ICMAB-CSIC. The authors acknowledge Servei de Microscòpia i Difracció de Raigs X from the Universitat Autònoma de Barcelona for the acquisition of cryo-TEM images.

References

1 W. R. Zipfel, R. M. Williams and W. W. Webb, Nonlinear Magic: Multiphoton Microscopy in the Biosciences, *Nat. Biotechnol.*, 2003, **21**(11), 1369–1377, DOI: 10.1038/nbt899.
2 W. Denk, J. H. Strickler and W. W. Webb, Two-Photon Laser Scanning Fluorescence Microscopy, *Science*, 1990, **52**(13 Suppl), 1778–1779, DOI: 10.1126/SCIENCE.2321027.
3 F. Helmchen and W. Denk, Deep Tissue Two-Photon Microscopy, *Nat. Methods*, 2005, **2**(12), 932–940, DOI: 10.1038/nmeth818.
4 A. Diaspro and M. Robello, Two-Photon Excitation of Fluorescence for Three-Dimensional Optical Imaging of Biological Structures, *J. Photochem. Photobiol. B Biol.*, 2000, **55**(1), 1–8, DOI: 10.1016/S1011-1344(00)00028-2.
5 P. T. C. So, C. Y. Dong, B. R. Masters and K. M. Berland, Two-Photon Excitation Fluorescence Microscopy, *Annu. Rev. Biomed. Eng.*, 2000, **2**, 399–429, DOI: 10.1146/ANNUREV.BIOENG.2.1.399.

Open Access Article. Published on 11 February 2026. Downloaded on 2/25/2026 7:32:26 AM.
This article is licensed under a Creative Commons Attribution-NonCommercial 3.0 Unported Licence.

6 S. Zhang, L. Liu, S. Ren, Z. Li, Y. Zhao, Z. Yang, R. Hu, J. Qu, S. Zhang, L. Liu, S. Ren, Z. Li, Y. Zhao, Z. Yang, R. Hu and J. Qu, Recent Advances in Nonlinear Optics for Bio-Imaging Applications, *Opto-Electron. Adv.*, 2020, **3**(10), 200003–2000031, DOI: 10.29026/OEA.2020.200003.

7 Y. M. Poronik, V. Hugues, M. Blanchard-Desce and D. T. Gryko, Octupolar Merocyanine Dyes: A New Class of Nonlinear Optical Chromophores, *Chem. – Eur. J.*, 2012, **18**(30), 9258–9266, DOI: 10.1002/CHEM.201200718.

8 S. Yao, H. Y. Ahn, X. Wang, J. Fu, E. W. Van Stryland, D. J. Hagan and K. D. Belfield, Donor-Acceptor-Donor Fluorene Derivatives for Two-Photon Fluorescence Lysosomal Imaging, *J. Org. Chem.*, 2010, **75**(12), 3965, DOI: 10.1021/JO100554J.

9 L. Mencaroni, C. Bonaccorso, V. Botti, B. Carlotti, G. Consiglio, F. Elisei, C. G. Fortuna, A. Spalletti and A. Cesaretti, Nonlinear Optical Properties of a New Panchromatic Series of Water-Soluble Bicationic Push-Pull Fluorophores, *Dyes Pigm.*, 2021, **194**, 109620, DOI: 10.1016/J.DYEPIG.2021.109620.

10 D. A. Parthenopoulos and P. M. Rentzepis, Three-Dimensional Optical Storage Memory, *Science*, 1989, **245**(4920), 843–845, DOI: 10.1126/SCIENCE.245.4920.843.

11 C. B. Nielsen, J. Arnbjerg, M. Johnsen, M. Joørgensen and P. R. Ogilby, Molecular Tuning of Phenylene-Vinylene Derivatives for Two-Photon Photosensitized Singlet Oxygen Production, *J. Org. Chem.*, 2009, **74**(23), 9094–9104, DOI: 10.1021/JO9020216.

12 S. Kawata, H. B. Sun, T. Tanaka and K. Takada, Finer Features for Functional Microdevices, *Nature*, 2001, **412**(6848), 697–698, DOI: 10.1038/35089130.

13 F. Terenziani, A. Painelli, C. Katan, M. Charlot and M. Blanchard-Desce, Charge Instability in Quadrupolar Chromophores: Symmetry Breaking and Solvatochromism, *J. Am. Chem. Soc.*, 2006, **128**(49), 15742–15755, DOI: 10.1021/JA064521J.

14 M. Pawlicki, H. A. Collins, R. G. Denning and H. L. Anderson, Two-Photon Absorption and the Design of Two-Photon Dyes, *Angew. Chem., Int. Ed.*, 2009, **48**(18), 3244–3266, DOI: 10.1002/anie.200805257.

15 F. Terenziani, C. Sissa and A. Painelli, Symmetry Breaking in Octupolar Chromophores: Solvatochromism and Electroabsorption, *J. Phys. Chem. B*, 2008, **112**(16), 5079–5087, DOI: 10.1021/JP710241G.

16 S. J. Chung, K. S. Kim, T. C. Lin, G. S. He, J. Swiatkiewicz and P. N. Prasad, Cooperative Enhancement of Two-Photon Absorption in Multi-Branched Structures, *J. Phys. Chem. B*, 1999, **103**(49), 10741–10745, DOI: 10.1021/JP992846Z.

17 Pragti, B. K. Kundu, R. Chen, J. Diao and Y. Sun, Near-Infrared Bioimaging Using Two-Photon Fluorescent Probes, *Adv. Healthcare Mater.*, 2025, **14**(3), 2403272, DOI: 10.1002/ADHM.202403272.

18 C. Han, B. K. Kundu, Y. Liang and Y. Sun, Near-Infrared Light-Driven Photocatalysis with an Emphasis on Two-Photon Excitation: Concepts, Materials, and Applications, *Adv. Mater.*, 2024, **36**(5), 2307759, DOI: 10.1002/ADMA.202307759.

19 C. Han, B. K. Kundu, R. Chen, N. Pragti, P. Srivastava, C. G. Elles and Y. Sun, Near-Infrared Light-Driven Condensation Using Branched Two-Photon-Absorbing Organic Photocatalysts with Viscosity-Dependent Properties, *J. Am. Chem. Soc.*, 2025, **147**(24), 20525–20533, DOI: 10.1021/JACS.5C02797.

20 Y. Wan, W. Chen, Y. Liu, K. W. Lee, Y. Gao, D. Zhang, Y. Li, Z. Huang, J. Luo, C. S. Lee and S. Li, Neutral Cyanine: Ultra-Stable NIR-II Merocyanines for Highly Efficient Bioimaging and Tumor-Targeted Phototheranostics, *Adv. Mater.*, 2024, **36**(31), 2405966, DOI: 10.1002/ADMA.202405966.

21 J. Hoche, A. Schulz, L. M. Dietrich, A. Humeniuk, M. Stolte, D. Schmidt, T. Brixner, F. Würthner and R. Mitric, The Origin of the Solvent Dependence of Fluorescence Quantum Yields in Dipolar Merocyanine Dyes, *Chem. Sci.*, 2019, **10**(48), 11013–11022, DOI: 10.1039/C9SC05012D.

22 G. Vargas-Nadal, M. Köber, A. Nsamela, F. Terenziani, C. Sissa, S. Pescina, F. Sonvico, A. M. Gazzali, H. A. Wahab, L. Grisanti, M. E. Olivera, M. C. Palena, M. L. Guzman, L. C. Luciani-Giacobbe, A. Jimenez-Kairuz, N. Ventosa, I. Ratera, K. D. Belfield and B. M. Maoz, Fluorescent Multifunctional Organic Nanoparticles for Drug Delivery and Bioimaging: A Tutorial Review, *Pharmaceutics*, 2022, **14**(11), 2498, DOI: 10.3390/PHARMACEUTICS14112498.

23 A. Reisch and A. S. Klymchenko, Fluorescent Polymer Nanoparticles Based on Dyes: Seeking Brighter Tools for Bioimaging, *Small*, 2016, **12**(15), 1968, DOI: 10.1002/SMLL.201503396.

24 L. Ferrer-Tasies, E. Moreno-Calvo, M. Cano-Sarabia, M. Aguilella-Arzo, A. Angelova, S. Lesieur, S. Ricart, J. Faraudo, N. Ventosa and J. Veciana, Quatsomes: Vesicles Formed by Self-Assembly of Sterols and Quaternary Ammonium Surfactants, *Langmuir*, 2013, **29**(22), 6519–6528, DOI: 10.1021/LA4003803.

25 M. Köber, S. Illa-Tuset, L. Ferrer-Tasies, E. Moreno-Calvo, W. I. Tatkiewicz, N. Grimaldi, D. Piña, A. P. Pérez, V. Lloveras, J. Vidal-Gancedo, D. Bulone, I. Ratera, J. S. Pedersen, D. Danino, J. Veciana, J. Faraudo and N. Ventosa, Stable Nanovesicles Formed by Intrinsically Planar Bilayers, *J. Colloid Interface Sci.*, 2023, **631**, 202–211, DOI: 10.1016/J.JCIS.2022.10.104.

26 C. Du, S. Woolcott, A. S. Wahba, S. R. Hamry, W. L. Odette, C. J. Thibodeaux, P. Marchand and J. Mauzeroll, Evaluation of Quatsome Morphology, Composition, and Stability for Pseudomonas Aeruginosa Biofilm Eradication, *Langmuir*, 2024, **40**(3), 1623–1632, DOI: 10.1021/ACS.LANGMUIR.3C02491.

27 M. Alcaina-Hernando, I. Malvacio, I. Ferraboschi, C. Huck-Iriart, A. Bianchera, S. Sala, J. S. Pedersen, L. Ferrer-Tasies, S. Pescina, C. Sissa, N. Ventosa and A. Córdoba, A New Plant-Based Drug Delivery Platform Based on Alkyl Polyglucosides and β-Sitosterol Nanovesicles for Topical Delivery, *Appl. Mater. Today*, 2024, **41**, 102467, DOI: 10.1016/J.APMT.2024.102467.

28 A. Boloix, N. Feiner-Gracia, M. Köber, J. Repetto, R. Pascarella, A. Soriano, M. Masanas, N. Segovia, G. Vargas-Nadal, J. Merlo-Mas, D. Danino, I. Abutbul-Ionita, L. Foradada, J. Roma, A. Córdoba, S. Sala, J. S. de Toledo, S. Gallego, J. Veciana, L. Albertazzi, M. F. Segura and N. Ventosa, Engineering PH-Sensitive Stable Nanovesicles for Delivery of MicroRNA Therapeutics, *Small*, 2022, **18**(3), 2101959, DOI: 10.1002/SMLL.202101959.

 This journal is © The Royal Society of Chemistry 2026

Open Access Article. Published on 11 February 2026. Downloaded on 2/25/2026 7:32:26 AM.
This article is licensed under a Creative Commons Attribution-NonCommercial 3.0 Unported Licence.

29 G. Vargas-Nadal, M. Muñoz-Ubeda, P. Alamo, M. M. Arnal, V. Céspedes, M. Köber, E. Gonzalez, L. Ferrer-Tasies, M. P. Vinardell, R. Mangues, J. Veciana and N. Ventosa, MKC-Quatsomes: A Stable Nanovesicle Platform for Bio-Imaging and Drug-Delivery Applications, *J. Nanomed. Nanotechnol.*, 2020, **24**, 102136, DOI: 10.1016/J.NANO.2019.102136.

30 L. Ferrer-Tasies, H. Santana, I. Cabrera-Puig, E. González-Mira, L. Ballell-Hosa, C. Castellar-Álvarez, A. Córdoba, J. Merlo-Mas, H. Gerónimo, G. Chinea, V. Falcón, E. Moreno-Calvo, J. S. Pedersen, J. Romero, C. Navarro-Requena, C. Valdés, M. Limonta, J. Berlanga, S. Sala, E. Martínez, J. Veciana and N. Ventosa, Recombinant Human Epidermal Growth Factor/Quatsome Nanoconjugates: A Robust Topical Delivery System for Complex Wound Healing, *Adv. Ther.*, 2021, **4**(6), 2000260, DOI: 10.1002/ADTP.202000260.

31 M. Rossetti, L. Stella, J. Morlà-Folch, S. Bobone, A. Boloix, L. Baranda, D. Moscone, M. Roldán, J. Veciana, M. F. Segura, M. Köber, N. Ventosa and A. Porchetta, Engineering DNA-Grafted Quatsomes as Stable Nucleic Acid-Responsive Fluorescent Nanovesicles, *Adv. Funct. Mater.*, 2021, **31**(46), 2103511, DOI: 10.1002/ADFM.202103511.

32 X. Liu, A. Ardizzone, B. Sui, M. Anzola, N. Ventosa, T. Liu, J. Veciana and K. D. Belfield, Fluorenyl-Loaded Quatsome Nanostructured Fluorescent Probes, *ACS Omega*, 2017, **2**(8), 4112–4122, DOI: 10.1021/ACSOMEGA.7B00779.

33 N. Bordignon, M. Köber, G. Chinigò, C. Pontremoli, E. Sansone, G. Vargas-Nadal, M. J. Moran Plata, A. Fiorio Pla, N. Barbero, J. Morla-Folch and N. Ventosa, Quatsomes Loaded with Squaraine Dye as an Effective Photosensitizer for Photodynamic Therapy, *Pharmaceutics*, 2023, **15**(3), 902, DOI: 10.3390/PHARMACEUTICS15030902.

34 A. Ardizzone, D. Blasi, D. Vona, A. Rosspeintner, A. Punzi, E. Altamura, N. Grimaldi, S. Sala, E. Vauthey, G. M. Farinola, I. Ratera, N. Ventosa and J. Veciana, Highly Stable and Red-Emitting Nanovesicles Incorporating Lipophilic Diketopyrrolopyrroles for Cell Imaging, *Chem. – Eur. J.*, 2018, **24**(44), 11386–11392, DOI: 10.1002/CHEM.201801444.

35 A. Ardizzone, S. Kurhuzenkau, S. Illa-Tuset, J. Faraudo, M. Bondar, D. Hagan, E. W. Van Stryland, A. Painelli, C. Sissa, N. Feiner, L. Albertazzi, J. Veciana and N. Ventosa, Nanostructuring Lipophilic Dyes in Water Using Stable Vesicles, Quatsomes, as Scaffolds and Their Use as Probes for Bioimaging, *Small*, 2018, **14**(16), 1703851, DOI: 10.1002/SMLL.201703851.

36 J. Morla-Folch, G. Vargas-Nadal, E. Fuentes, S. Illa-Tuset, M. Köber, C. Sissa, S. Pujals, A. Painelli, J. Veciana, J. Faraudo, K. D. Belfield, L. Albertazzi and N. Ventosa, Ultrabright Föster Resonance Energy Transfer Nanovesicles: The Role of Dye Diffusion, *Chem. Mater.*, 2022, **34**(19), 8517–8527, DOI: 10.1021/ACS.CHEMMATER.2C00384.

37 J. Morla-Folch, G. Vargas-Nadal, T. Zhao, C. Sissa, A. Ardizzone, S. Kurhuzenkau, M. Köber, M. Uddin, A. Painelli, J. Veciana, K. D. Belfield and N. Ventosa, Dye-Loaded Quatsomes Exhibiting FRET as Nanoprobes for Bioimaging, *ACS Appl. Mater. Interfaces*, 2020, **12**(18), 20253–20262, DOI: 10.1021/ACSAMI.0C03040.

38 A. Nowak-Król, R. Plamont, G. Canard, J. A. Edzang, D. T. Gryko and T. Balaban, An Efficient Synthesis of Porphyrins with Different Meso Substituents That Avoids Scrambling in Aqueous Media, *Chem. – Eur. J.*, 2015, **21**(4), 1488–1498, DOI: 10.1002/CHEM.201403677.

39 M. Bregnhøj, F. M. Pimenta, Y. M. Poronik, D. T. Gryko and P. R. Ogilby, Subtle Structural Changes in Octupolar Merocyanine Dyes Influence the Photosensitized Production of Singlet Oxygen, *Photochem. Photobiol. Sci.*, 2015, **14**(6), 1138–1146, DOI: 10.1039/C5PP00080G.

40 F. Terenziani, C. Sissa and A. Painelli, Symmetry Breaking in Octupolar Chromophores: Solvatochromism and Electroabsorption, *J. Phys. Chem. B*, 2008, **112**(16), 5079–5087, DOI: 10.1021/JP710241G.

41 I. Cabrera, E. Elizondo, O. Esteban, J. L. Corchero, M. Melgarejo, D. Pulido, A. Córdoba, E. Moreno, U. Unzueta, E. Vazquez, I. Abasolo, S. Schwartz, A. Villaverde, F. Albericio, M. Royo, M. F. García-Parajo, N. Ventosa and J. Veciana, Multifunctional Nanovesicle-Bioactive Conjugates Prepared by a One-Step Scalable Method Using CO_2-Expanded Solvents, *Nano Lett.*, 2013, **13**(8), 3766–3774, DOI: 10.1021/NL4017072.

42 M. Cano-Sarabia, N. Ventosa, S. Sala, C. Patiño, R. Arranz and J. Veciana, Preparation of Uniform Rich Cholesterol Unilamellar Nanovesicles Using CO_2-Expanded Solvents, *Langmuir*, 2008, **24**(6), 2433–2437, DOI: 10.1021/LA7032109.

43 N. Ventosa, J. Veciana and S. Sala, M. C. Method for Obtaining Micro- and Nano-Disperse Systems, WO2006079889A1, 2006.

44 F. C. Spano, The Spectral Signatures of Frenkel Polarons in H- And J-Aggregates, *Acc. Chem. Res.*, 2010, **43**(3), 429–439, DOI: 10.1021/AR900233V.

45 F. Bertocchi, A. Delledonne, G. Vargas-Nadal, F. Terenziani, A. Painelli and C. Sissa, Aggregates of Cyanine Dyes: When Molecular Vibrations and Electrostatic Screening Make the Difference, *J. Phys. Chem. C*, 2023, **127**(21), 10185–10196, DOI: 10.1021/ACS.JPCC.3C01253.

46 M. Bregnhøj, F. M. Pimenta, Y. M. Poronik, D. T. Gryko and P. R. Ogilby, Subtle Structural Changes in Octupolar Merocyanine Dyes Influence the Photosensitized Production of Singlet Oxygen, *Photochem. Photobiol. Sci.*, 2015, **14**(6), 1138–1146, DOI: 10.1039/C5PP00080G/METRICS.

47 A. Hajda, R. Guha, S. M. Copp and J. Olesiak-Bańska, Two-Photon Brightness of NIR-Emitting, Atomically Precise DNA-Stabilized Silver Nanoclusters, *Chem. Sci.*, 2025, **16**(4), 1737–1745, DOI: 10.1039/D4SC05853D.

48 W. W. Webb, M. A. Albota and C. Xu, Two-Photon Fluorescence Excitation Cross Sections of Biomolecular Probes from 690 to 960 Nm, *Appl. Opt.*, 1998, **37**(31), 7352–7356, DOI: 10.1364/AO.37.007352.

49 E. J. Ngen, L. Xiao, P. Rajaputra, X. Yan and Y. You, Enhanced Singlet Oxygen Generation from a Porphyrin–Rhodamine B Dyad by Two-Photon Excitation through Resonance Energy Transfer, *Photochem. Photobiol.*, 2013, **89**(4), 841–848, DOI: 10.1111/PHP.12071.

50 S. Nicoli, G. Ferrari, M. Quarta, C. Macaluso, P. Govoni, D. Dallatana and P. S. Porcine, Sclera as a Model of Human

Open Access Article. Published on 11 February 2026. Downloaded on 2/25/2026 7:32:26 AM.
This article is licensed under a Creative Commons Attribution-NonCommercial 3.0 Unported Licence.

Sclera for in Vitro Transport Experiments: Histology, SEM, and Comparative Permeability, *Methods Mol. Biol.*, 2019, **1834**, 333, DOI: 10.1007/978-1-4939-8669-9_21.

51 M. Spedicati, G. Ruocco, A. Zoso, L. Mortati, A. Lapini, A. Delledonne, C. Divieto, V. Romano, C. Castaldo, F. Di Meglio, D. Nurzynska, I. Carmagnola and V. Chiono, Biomimetic Design of Bioartificial Scaffolds for the in Vitro Modelling of Human Cardiac Fibrosis, *Front. Bioeng. Biotechnol.*, 2022, **10**, 983872, DOI: 10.3389/FBIOE.2022.983872.

52 A. Delledonne, E. Guazzelli, S. Pescina, A. Bianchera, G. Galli, E. Martinelli and C. Sissa, Amphiphilic Fluorinated Unimer Micelles as Nanocarriers of Fluorescent Probes for Bioimaging, *ACS Appl. Nano Mater.*, 2023, **6**(17), 15551–15562, DOI: 10.1021/ACSANM.3C02300.

53 W. R. Zipfel, R. M. Williams, W. W. Webb and I. Freund, Second Harmonic Generation Imaging of Collagen Fibrils in Cornea and Sclera, *Opt. Express*, 2005, **13**(15), 5791–5797, DOI: 10.1364/OPEX.13.005791.

54 C. Le Droumaguet, A. Sourdon, E. Genin, O. Mongin and M. Blanchard-Desce, Two-Photon Polarity Probes Built from Octupolar Fluorophores: Synthesis, Structure-Properties Relationships, and Use in Cellular Imaging, *Chem. – Asian J.*, 2013, **8**(12), 2984–3001, DOI: 10.1002/ASIA.201300735.

55 M. J. Frisch, G. W. Trucks, H. B. Schlegel, G. E. Scuseria, M. A. Robb, J. R. Cheeseman, G. Scalmani, V. Barone, G. A. Petersson, H. Nakatsuji, X. Li, M. Caricato, A. V. Marenich, J. Bloino, B. G. Janesko, R. Gomperts, B. Mennucci, H. P. Hratchian, J. V and D. J. F, *Gaussian 16, Revision B.01.*, Gaussian, Inc., Wallingford CT, 2016.

56 A. Rebane, S. Reguardati, J. de; Pahapill, Y. Stepanenko and A. Mikhailov, High-Accuracy Reference Standards for Two-Photon Absorption in the 680-1050 Nm Wavelength Range, *Opt. Express*, 2016, **24**(8), 9053–9066, DOI: 10.1364/OE.24.009053.

 This journal is © The Royal Society of Chemistry 2026